Remote Sensing of Environment 302 (2024) 113983

Contents lists available at ScienceDirect

Remote Sensing of Environment

journal homepage: www.elsevier.com/locate/rse

Evaluation of three contrasting models in estimating primary production from ocean color remote sensing using long-term time-series data at oceanic and coastal sites

Jinghui Wu[a,*], Zhongping Lee[b,*], Joaquim Goes[a], Helga do Rosario Gomes[a], Jianwei Wei[c,d]

[a] Lamont Doherty Earth Observatory at Columbia University, Palisades, NY, USA
[b] State Key Lab of Marine Environmental Science, College of Ocean and Earth Sciences, Xiamen University, Xiamen, China
[c] NOAA/NESDIS Center for Satellite Applications and Research, College Park, MD, USA
[d] Global Science & Technology, Inc., Greenbelt, MD 20770, USA

ARTICLE INFO

Editor: Menghua Wang

Keywords:
Net primary production
Ocean color remote sensing
Time-series
HOT, BATS, CARIACO

ABSTRACT

Accurate estimates of depth-integrated Net Primary Production (NPP, mg C m^{-2} d^{-1}) and the creation of a robust climate data record of NPP for the global oceans are essential goals of the ocean color remote sensing community. Here, we take advantage of *in situ* NPP measurements from three long-term time-series sites, the HOT (Hawaii Ocean Time-series), BATS (Bermuda Atlantic Time-series Study) and CARIACO (Ocean Time-Series Program from the Cariaco basin), spanning over 30 years to evaluate three contrasting models in estimating NPP from ocean color remote sensing. These models for NPP estimation include the Absorption-based Model (AbPM), which relies on phytoplankton absorption coefficient, the Vertically Generalized Production Model (VGPM), which centers on chlorophyll-a concentration, and the Carbon-based Productivity Model (CbPM) centering on phytoplankton carbon. In addition to the accuracy of NPP estimation from these models, we laid great emphasis on evaluating their skills in capturing the monthly to seasonal variations and interannual trends in NPP at the three sites. Comparison with *in situ* NPP at all three long-term sites (~20 years) showed that AbPM yielded the highest coefficient of determination (R^2 = 0.67) and the lowest uncertainties (Bias = 0.03 and unbiased root mean square difference = 0.17). Seasonal and interannual variations apparent in the *in situ* NPP time-series records were best captured by AbPM. These results showcase the robust capabilities of AbPM and its superiority for global carbon cycling and climate change studies, largely because it takes into account optical and photosynthetic parameters of local phytoplankton.

1. Introduction

Phytoplankton Net Primary Production (NPP, mg C m^{-2} d^{-1}), a measure of carbon biomass production resulting from photosynthesis, is responsible for almost half of the global annual NPP (~50 × 10^{15} g C yr^{-1}). This process within the base of the marine food web (Field et al., 1998) plays a critical role in the global carbon cycle, helping to sequester CO_2 from the atmosphere to the deep ocean *via* the "biological pump" (Eppley and Renger, 1988; Eppley and Peterson, 1979; Falkowski, 1994; Le Quéré et al., 2018). For this reason, estimating the temporal, spatial and long-term variations of NPP in the water column is central to understanding the impacts of climate and human-induced changes on the global carbon cycle (Doney et al., 2009; Gruber et al., 2019; Keeling et al., 2009; Reid et al., 2009) as well as the oceans' role in regulating the earth climate (Boyd et al., 2019).

Conventionally, *in situ* NPP (NPP_{insitu}) measurements have been largely from research cruises, which are sporadic and scattered, limiting their spatial and temporal coverages for global and climate scale studies. The launch of ocean color satellites since the late 1970s provided multispectral measurements of ocean waters (ocean color) and, subsequently, satellite products that led to the development of novel approaches for estimating NPP from space (Brewin et al., 2023; Perry, 1986; Westberry et al., 2023). Despite much progress, accurate estimates of NPP from satellite ocean color data are, however, contingent upon the methodological approach, and the satellite data products being used for scaling limited shipboard data to regional, basin and global scales (Eppley et al.,

* Corresponding authors.
E-mail addresses: jinghuiw@ldeo.columbia.edu (J. Wu), zhongping.lee@umb.edu (Z. Lee), jig@ldeo.columbia.edu (J. Goes), helga@ldeo.columbia.edu (H.R. Gomes), jianwei.wei@noaa.gov (J. Wei).

https://doi.org/10.1016/j.rse.2023.113983
Received 12 March 2023; Received in revised form 21 December 2023; Accepted 23 December 2023
Available online 12 January 2024

Table 1
Symbols and abbreviations used in this article.

Symbol	Definition	Units
AbPM	The Absorption-based model	–
$a_{ph}(443)$	Phytoplankton absorption coefficient at 443 nm	m^{-1}
BATS	Bermuda Atlantic Time series Study	–
$b_{bp}(443)$	Particle backscattering coefficients at 443 nm	m^{-1}
CARIACO	CArbon Retention In A Colored Ocean Time-Series	–
CbPM	Carbon-based Productivity Model	–
Chla	Chlorophyll a concentration	$mg\ m^{-3}$
C_{phy}	Phytoplankton carbon stock	$mg\ m^{-3}$
HOT	Hawaii Ocean Time-series	–
I_{ML}	Median mixed layer light level	mol photons $m^{-2}\ h^{-1}$
$K_d(\lambda)$	Attenuation coefficient of downwelling irradiance	m^{-1}
K_ϕ	Irradiance when φ corresponds to a half of ϕ_m	mol photons $m^{-2}\ d^{-1}$
MLD	Mixed layer depth	m
NPP	Net Primary Production	$mg\ C\ m^{-2}\ d^{-1}$
NPP_{AbPM}	NPP from AbPM using OC-CCI as primary input data	$mg\ C\ m^{-2}\ d^{-1}$
NPP_{CbPM}	NPP from CbPM using OC-CCI as primary input data	$mg\ C\ m^{-2}\ d^{-1}$
NPP_{insitu}	NPP from *in situ* measurements	$mg\ C\ m^{-2}\ d^{-1}$
NPP_{model}	NPP from models	$mg\ C\ m^{-2}\ d^{-1}$
NPP_{VGPM}	NPP from VGPM using OC-CCI as primary input data	$mg\ C\ m^{-2}\ d^{-1}$
OC-CCI	Ocean Color Climate Change Initiative project	–
PAR_{day}	Photosynthetic available radiation	mol photons $m^{-2}\ d^{-1}$
P^B_{opt}	Maximum carbon fixation rate within the water column normalized by *Chla*	$mg\ C\ mg\ Chl^{-1}\ h^{-1}$
ϕ	Quantum yield of phytoplankton photosynthesis	mol C mol $photons^{-1}$
ϕ_m	Maximum quantum yield of phytoplankton photosynthesis	mol C mol $photons^{-1}$
$R_{rs}(\lambda)$	Remote sensing reflectance	sr^{-1}
SST	Sea surface temperature	°C
μ	Growth rate of phytoplankton	d^{-1}
VGPM	Vertically Generalized Production Model	–
Z_{eu}	Euphotic zone depth	m
Z_{NO3}	Nitracline depths	m

1985; Falkowski, 1998; Perry, 1986; Platt, 1986).

There have been many models developed for estimating NPP (NPP_{model}) from satellite measurements (Behrenfeld and Falkowski, 1997; Lee et al., 2011; Morel, 1991; Platt and Sathyendranath, 1988; Westberry et al., 2008), which in general can be grouped into two categories based on the satellite product used. The first are the biomass-based models, which rely on either 1) chlorophyll *a* concentration (*Chla*; please see Table 1 for symbols, definitions, and units for all relevant parameters) or Chl-based models (Behrenfeld and Falkowski, 1997; Brewin et al., 2021; Platt and Sathyendranath, 1988; Sathyendranath and Platt, 1995) or on, 2) phytoplankton carbon (C_{phy}) concentrations or C_{phy}-based models (Behrenfeld et al., 2005; Westberry et al., 2008). The second category is biomass independent models which instead rely on the absorption coefficient of phytoplankton (a_{ph}) or a_{ph}-based models (Barnes et al., 2014; Hirawake et al., 2011; Lee et al., 2011; Lee et al., 1996; Marra et al., 2003). Over the past decades, the most commonly used NPP models have relied on *Chla* estimates from space (Behrenfeld and Falkowski, 1997; Platt and Sathyendranath, 1988; Sathyendranath and Platt, 1995), with the Vertically Generalized Production Model (VGPM) (Behrenfeld and Falkowski, 1997) being the most popular, in part due to its simplicity and ease of use.

In recognition of the uncertainties associated with satellite *Chla* estimates (Behrenfeld et al., 2005; Saba et al., 2011), and the difficulties in accurately estimating the maximum biomass-normalized phytoplankton photosynthesis rates, Behrenfeld et al. (2005) developed the C_{phy}-based model (referred hereinafter as the CbPM) that utilizes phytoplankton carbon (C_{phy}, converted from particle backscattering coefficient, b_{bp}) for the estimation of NPP. As compared to the empirical inversion of *Chla* from ocean color, both b_{bp} and a_{ph} can be retrieved analytically or semi-analytically from ocean color (Lee et al., 2002; Werdell et al., 2013), thus in theory, the newer models based on b_{bp} and a_{ph} (hereinafter referred to as AbPM) should be capable of providing more accurate estimates of oceanic NPP from space.

Over the last several years, NPP models, in particular those that have relied on satellite *Chla*, have helped provide estimates of annual global oceanic NPP that range from ~36.5 to 67 (48.2 ± 8) Pg C yr^{-1} (Carr et al., 2006), and carbon export rates ranging from ~5 to over 12 Pg C yr^{-1} (Boyd and Trull, 2007; Henson et al., 2011). These estimates are however beset by large uncertainties, which at times can exceed the annual anthropogenic CO_2 emission rates of ~7 to 11 Pg C yr^{-1} (Siegel et al., 2014), thus precluding their use for assessing the role of the oceans in the global carbon cycle or for estimating ocean biological carbon drawdown and its evolution under future climate scenarios (Friedrichs et al., 2009; Regaudie-de-Gioux et al., 2019; Saba et al., 2011; Saba et al., 2010). This situation demands that we continue to develop, test and refine satellite models to obtain more reliable NPP estimates that can provide more robust assessments of the magnitude and the trends in NPP over seasonal, annual to multidecadal time periods that are useful for climate change studies.

Previous attempts at comparing the performances of various NPP models including individual studies (Lee et al., 2015a; Lee et al., 2011; Regaudie-de-Gioux et al., 2019) and group efforts such as the community Primary Productivity Algorithm Round Robin (PPARR) workshops organized by NASA (Campbell et al., 2002; Carr et al., 2006; Friedrichs et al., 2009; Saba et al., 2011; Saba et al., 2010), where NPP_{insitu} data from both coastal and open ocean locations were utilized to evaluate the accuracy of NPP_{model}. A major revelation from these model comparison efforts is that most models differed in their skills in accurately representing NPP_{insitu} (Kahru, 2017) within optically complex coastal waters (Saba et al., 2011) and in oligotrophic oceans (Friedrichs et al., 2009; Regaudie-de-Gioux et al., 2019; Shih et al., 2021). Furthermore, it was observed that several NPP models appeared incapable of accurately capturing the seasonal, annual and long-term trends seen in field measurements of NPP, precluding their use as a means for predicting future NPP variability under different environment and climate scenarios (Chavez et al., 2011; Dave and Lozier, 2010; Ducklow et al., 2009).

With the development and refinement of CbPM (Westberry et al., 2008) and AbPM (Barnes et al., 2014; Lee et al., 2011; Lee et al., 1996), NPP estimates from ocean color data have seen marked improvement over conventional Chl-based PP models (Kahru, 2017; Lee et al., 2011). However, we deemed it necessary to evaluate if these two new approaches could better capture the magnitude as well as the temporal and/or long-term trends in NPP required for climate change studies than that possible by Chl-based NPP models. In this study, we relied on a nearly 30-year time-series of NPP_{insitu} from two oceanic sites (Hawaii Ocean Time-series, HOT, in the North Pacific, and Bermuda Atlantic Time-series Study, BATS, in North Atlantic) and a coastal site (CARIACO, an Ocean Time-Series Program located in upwelling waters of the Cariaco basin) to evaluate the performance of AbPM and CbPM, against VGPM - one of the more widely used Chl-based models.

2. NPP models

2.1. Chl-based model: VGPM

The Vertically Generalized Production Model (VGPM) developed by Behrenfeld and Falkowski (1997) that uses *Chla* as an input parameter has been, over the past 20+ years, the most popular model for estimating NPP from ocean color measurements. Despite some of its inherent limitations recently detailed in Lee and Marra (2022), it has undoubtedly greatly influenced our understanding of biological and biogeochemical ocean process studies over the past two decades.

For VGPM, integrated primary production within the euphotic zone is expressed as,

$$NPP_{VGPM} = 0.66125 \times P_{opt}^{B} \times \frac{PAR_{day}}{PAR_{day} + 4.1} \times Z_{eu} \times Chla \times DL \quad (1)$$

where $P_{\text{opt}}^{\text{B}}$ (in mg C (mg Chl)$^{-1}$ h^{-1}) is the maximum carbon fixation rate of the water column normalized by *Chla*, PAR_{day} is the daily photosynthetic available radiation (mol photons m^{-2} d^{-1}), Z_{eu} (m) is the euphotic zone depth, and DL is the day length (in hours). *Chla*, PAR_{day} and Z_{eu} are available or derived from ocean color measurements. $P_{\text{opt}}^{\text{B}}$ was originally modeled as a polynomial function of sea-surface temperature (SST) (Behrenfeld and Falkowski, 1997), here we used the updated Eppley-VGPM, where $P_{\text{opt}}^{\text{B}}$ was modeled as an exponential function of temperature (Morel, 1991), obtained based on the temperature-dependent growth function presented in Eppley (1972). The rationale behind selecting Eppley-VGPM is based on its better performance compared to the original VGPM, as substantiated in previous studies (Friedland et al., 2012; Zhang et al., 2018). While global NPP products based on Eppley-VGPM (and CbPM) are available for download at the model developers' website (http://orca.science.oregonstate.edu/npp_products.php), we found that the differences between these products and the *in situ* NPP measurements at the three time-series sites were large (see Fig. S1 in Supplementary Materials). Since the NPP estimates obtained with the code are better than those derived from the online data products, our estimates of NPP at the three sites are based on our application of the code to satellite ocean color and other data products as described in more detail below.

2.2. C_{phy}-based model: CbPM

Recognizing that phytoplankton respond to changes in light, nutrients, and temperature by adjusting cellular pigment levels and that this response can be quantified by changes in the ratio of chlorophyll to carbon biomass (*Chla*:C_{phy}), Behrenfeld et al. (2005) developed CbPM wherein phytoplankton carbon (C_{phy}) replaced *Chla* as a key input, and this model was subsequently refined by Westberry et al. (2008).

For CbPM, NPP is the product of C_{phy} and the growth rate of phytoplankton (μ, d^{-1}), with C_{phy} estimated from particle backscattering coefficient at 443 nm ($b_{\text{bp}}(443)$, m^{-1}), and μ is estimated using μ_{max}, *Chla*:C_{phy} and the median mixed layer light level (I_{ML}, mol photons m^{-2} h^{-1}). Conceptually NPP estimated by CbPM can be expressed as:

$$NPP_{CbPM} = C_{phy} \times \mu\{\mu_{max}, Chla : C_{phy}, I_{ML}\} \quad (2)$$

where μ_{max} is the maximum daily growth rate taken as 2 d^{-1}, while I_{ML} is the light level at half depth of the mixed layer, which is calculated from PAR at surface (PAR(0)) and the diffuse attenuation coefficient of downwelling irradiance ($K_{\text{d}}(490)$, in m^{-1}). The required input parameters, $b_{\text{bp}}(443)$, *Chla*, PAR(0) and $K_{\text{d}}(490)$ are available from satellite ocean color measurements, while the mixed layer depth (MLD, m) and the nitracline (Z_{NO3}, m) depths are obtained from climatological data or model outputs. The code for NPP calculation following CbPM was also downloaded from Oregon State University's webpage (http://sites.science.oregonstate.edu/ocean.productivity/cbpm2.code.php).

2.3. a_{ph}-based model: AbPM

a_{ph}-based NPP model relies primarily on the absorbed solar radiation by phytoplankton and its conversion to organic carbon or primary production, which can be expressed as (Antoine and Morel, 1996; Kiefer and Mitchell, 1983; Lee et al., 1996):

$$NPP_{AbPM} = E_{abs} \times \phi \quad (3)$$

Here E_{abs} represents absorbed solar radiation by phytoplankton, while ϕ is the quantum yield of phytoplankton photosynthesis (mol C (mol photons)$^{-1}$) or the efficiency with which absorbed energy is converted into organic carbon. For depth-resolved AbPM, E_{abs} is

$$E_{abs}(z) = \int_{400}^{700} a_{ph}(\lambda) \times E_{day}(z,\lambda) d\lambda \quad (4)$$

where $a_{\text{ph}}(\lambda)$ from 400 to 700 nm can be estimated from $a_{\text{ph}}(443)$ using a model presented in Lee et al. (1999), and wavelength step (dλ) for the integration is 5 nm, here we assumed $a_{\text{ph}}(\lambda)$ is constant over the euphotic zone. $E_{\text{day}}(z,\lambda)$ is daily irradiance (mol photons m^{-2} d^{-1}) for wavelength λ (nm) at depth z, which can be calculated from $E_{\text{day}}(0^{-},\lambda)$ and $K_{\text{d}}(\lambda)$ as follows:

$$E_{day}(z,\lambda) = E_{day}(0^{-},\lambda) \bullet e^{-K_d(\lambda)\times z} \quad (5)$$

Details for obtaining $E_{\text{day}}(0^{-},\lambda)$ and $E_{\text{day}}(z,\lambda)$ can be found in Zoffoli et al. (2018) and Wu et al. (2022).

The vertical variation of ϕ is modeled as (Lee et al., 2011; Lee et al., 1996):

$$\phi(z) = \phi_{\text{m}} \times \frac{K_{\phi}}{K_{\phi} + PAR_{day}(z)} \times exp(-\nu \times PAR_{day}(z)) \quad (6)$$

where ϕ_{m} is the maximum quantum yield of photosynthesis, K_{ϕ} is a model parameter describing the reduction of ϕ under higher radiation, and ν is a parameter for photoinhibition. This model basically combines the Kiefer and Mitchell (1983) for ϕ under no photoinhibition, and with photoinhibition as indicated in Platt et al. (1980). Values of ϕ_{m}, K_{ϕ} and ν were taken as 0.06 mol C (mol photons)$^{-1}$ (Lee et al., 2011; Morel, 1991), 10.0 mol photons m^{-2} d^{-1} and 0.01 mol photons m^{-2} d^{-1} (Lee et al., 2011), respectively, and kept constant in this study. Note that a_{ph} required in Eq. (4) can be directly inverted from ocean color measurements (Lee et al., 2002; Werdell et al., 2013), and the integration of Eq. (3) over the euphotic zone depth then provides the NPP of the water column.

2.4. Metrics for model performance

In addition to regression analyses, the following metrics were employed to measure the performance of each model. These include the model-data fit in $\log_{10}$ space (Δ), the root mean square difference in $\log_{10}$ (RMSD; (Campbell et al., 2002)), the log normalized bias (*Bias*) and the unbiased RMSD (*u*RMSD), which are defined, respectively, as

$$\Delta(i) = log_{10}(NPP_{model}(i)) - log_{10}(NPP_{in\ situ}(i)) \quad (7)$$

with $\text{NPP}_{\text{model}}$ and NPP_{insitu} representing modeled and *in situ* NPP, respectively.

$$RMSD = \left(\frac{1}{N}\sum_{i=1}^{N}(log_{10}(NPP_{model}(i)) - log_{10}(NPP_{in\ situ}(i)))^{2}\right)^{0.5} \quad (8)$$

where N is the total number of paired data.

$$Bias = \overline{log_{10}(NPP_{model})} - \overline{log_{10}(NPP_{in\ situ})} \quad (9)$$

$$uRMSD = (RMSD^{2} - Bias^{2})^{0.5} \quad (10)$$

The upper bar in Eq. (9) represents the average, while negative or positive *Bias* indicates that the model underestimates or overestimates NPP compared to *in situ* measurements.

The median ratio value (Median ratio), semi-interquartile range (SIQR) and the median of the individual absolute percent difference (MPD) between each satellite and *in situ* input variable were calculated for each of the three time-series stations. For time-series analyses, the climatology of NPP was derived from monthly averages, while the annual average for the time-series was from the period of available satellite data (*i.e.*, Sep. 1997 to the last sampled date available for this study).

Additionally, a Target diagram (Jolliff et al., 2009) is used to illustrate model performance more intuitively. This diagram allows

Table 2
Input variables for the three NPP models evaluated.

Model	PAR	Z_{eu}	SST	$K_d(490)$	Chla	$a_{ph}(443)$	Z_{NO3}	$b_{bp}(443)$	MLD	Reference
AbPM	✓	✓		✓		✓				Lee et al. (1996, 2011)
VGPM	✓	✓	✓		✓					Behrenfeld and Falkowski (1997)
CbPM	✓	✓	✓	✓	✓		✓	✓	✓	Westberry et al. (2008)

Table 3
An evaluation of variables at the three time-series sites (HOT, BATS and CARIACO) between satellite products or model estimates and field measurements, where these variables are required for the NPP models.

Station	Statistics	*Chla*	PAR	SST	MLD
Unit		mg m^{-3}	mol photons m^{-2} d^{-1}	°C	m
	N	189	127	301	216
	R^2	0.07	0.70	0.91	0.55
HOT	Median Ratio	0.94	1.23	1.00	0.93
	SIQR	0.18	0.18	0.01	0.18
	MPD	19.0	6.2	0.8	19.5
	N	107	107	343	212
	R^2	0.04	0.63	0.96	0.74
BATS	Median Ratio	0.90	0.87	1.00	0.83
	SIQR	0.42	0.16	0.02	0.16
	MPD	43.0	4.8	1.5	22.2
	N	202	204	229	201
	R^2	0.55	0.91	0.85	0.40
CARIACO	Median Ratio	1.80	1.00	1.01	1.23
	SIQR	0.59	0.01	0.02	0.27
	MPD	81.0	1.0	1.9	24.3
	N	498	338	462	629
	R^2	0.57	0.71	0.94	0.74
Total	Median Ratio	1.10	1.01	1.00	0.98
	SIQR	0.46	0.19	0.01	0.20
	MPD	37.2	2.6	1.3	21.3

visualizing *Bias*, *u*RMSD and RMSD of all models in a single plot. For this purpose, the quantities are normalized by the standard deviation (σ_d) of $\log_{10}(NPP_{insitu})$, where a new set of metrics is calculated:

$$Bias^{*} = Bias/\sigma_d \tag{11}$$

$$uRMSD^{*} = sign(\sigma_m - \sigma_d) \times uRMSD/\sigma_d \tag{12}$$

Here σ_m is the standard deviation of $\log_{10}(NPP_{model})$.

A Target diagram provides information on if i) standard deviation from modeling is less or greater than that from *in situ* measurements; and ii) average value from modeling is less or greater than that from *in situ* measurements. The distance of each point from the origin is σ_d normalized-total RMSD (RMSD* = RMSD/σ_d). Any points greater than RMSD* = 1 are considered as poor performers.

The Target diagram primarily focuses on visualizing accuracy and precision, but a particular *u*RMSD value has limited information on correlations of the datasets or variation of the observations, making it less informative in that aspect. Unlike the Target diagram, the Taylor diagram (Taylor, 2001) provides a way of graphically summarizing how closely derived values (NPP_{model}) match observations (NPP_{insitu}). The similarity between two patterns is quantified in terms of their correlation, the centered root-mean-square difference and the amplitude of their variations (represented by their standard deviations). Thus Taylor diagrams complement Target diagrams by illustrating greater details about the difference in variability between modeled and observed data (Friedrichs et al., 2009).

Further, cosine similarity - the cosine of the angle between two vectors - is used to determine the similarity between two sets of data. For vectors A and B, the cosine similarity between them is calculated as:

$$\text{Cosine Similarity}(A, B) = (A \bullet B)/(\|A\|^{*}\|B\|) \tag{13}$$

where A • B represents the dot product of the two vectors. ||A|| and ||B|| are the magnitudes (lengths) of the vectors A and B, respectively. The resulting cosine similarity score will be a value between −1 and 1, with the score − 1 or 1 indicating perfect dissimilarity/similarity and 0 means no similarity. In summary, a higher score indicates greater similarity, while a lower score suggests dissimilarity.

We have also used the empirical cumulative distribution function (ECDF) to further visualize model performance. Although *Bias* provides a succinct measure of the magnitude and sign of model bias, it is not possible from this statistic alone to determine whether positive biases result from overestimating high values, low values, or both. ECDF clearly reveals where in the spectrum of values the biases occur, and is an excellent method for visualizing median, maximum and minimum values of datasets.

3. Datasets

3.1. Long-term time-series for in situ NPP measurements

Three decades of continuous *in situ* NPP measurements from three locations provide a superior data compilation for capturing temporal patterns in bio-geochemical properties over climate change scales compared to traditional short-term ship-based campaigns. As mentioned earlier, BATS (https://bats.bios.edu/) is located in the North Atlantic (31°40′N, 64°10′W), while HOT (https://hahana.soest.hawaii.edu/hot/hot_jgofs.html) is located in the subtropical North Pacific (22°45′N, 158°00′W). CARIACO (https://imars.usf.edu/CAR/index.html/), on the other hand, is located in the region of coastal upwelling in the Cariaco basin (10°30′N, 158°00′W). These time-series programs provide monthly and at times multiple datasets per month at the same location, where core oceanographic variables such as temperature, salinity, PAR, *Chla* and NPP at several depths in the euphotic zone have been measured. More importantly, these programs also provide remote sensing reflectance ($R_{rs}(\lambda)$) *via* radiometric measurements of ocean (water) color.

3.2. NPP_{insitu} for validation

A total of 306 NPP_{insitu} were obtained for the period 1988 to 2018 at HOT, 374 stations at BATS for the period from 1988 to 2016, and 231 stations at CARIACO from 1995 to 2015. Estimates of NPP at depth z (NPP(z), mg C m^{-3} d^{-1}) at these time-series locations are based on the ^{14}C-tracer methodology (Steemann Nielsen, 1952), with water samples taken from several depths in the water column and incubated with the tracer from dawn to dusk. All estimates of NPP(z) followed the community-accepted protocols described in the International JGOFS manual (Knap et al., 1996). Individual NPP measurements were corrected for dark ^{14}C uptake. Daily water-column integrated NPP (NPP_{insitu}, mg C m^{-2} d^{-1}) was calculated by the trapezoidal integration of measured NPP(z) from the surface (sampling depth is 0 to 10 m) to Z_{eu} (Church et al., 2013; D'Alelio et al., 2020; Muller-Karger et al., 2019), which is defined here as the depth of 1% of surface PAR, although a more representative Z_{eu} approximates 0.5% of surface PAR (Wu et al., 2021). While these long-term *in situ* NPP at the three stations are used in the following as the reference to evaluate the three NPP models, it is necessary to keep in mind that as all field measurements, these *in situ* NPP also contains uncertainties (Marra, 2002).

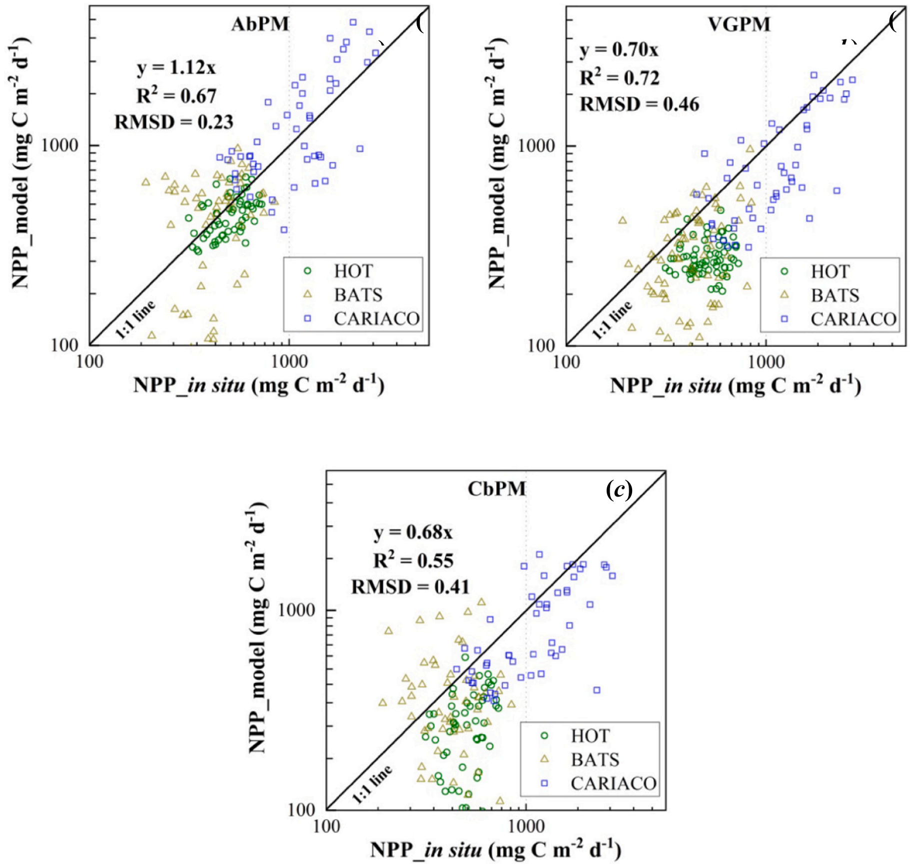

Fig. 1. Comparison between NPP_{insitu} ($N = 160$) from HOT ($N = 57$), BATS ($N = 55$) and CARIACO ($N = 48$) and NPP_{model} derived using major inputs estimated from *in situ* R_{rs} for (*a*) AbPM, (*b*) VGPM, and (*c*) CbPM.

3.2.1. HOT

At HOT, all incubations for NPP(z) from 1990 through mid-2000 were conducted *in situ*, using water samples drawn from 0 to 175 m collected at intervals of 20–30 m. Incubations were undertaken from dawn to dusk (10 to 16 h) using a free-drifting array. Generally, the average value of NPP in the light bottles ($N = 3$) was dark bottle corrected to exclude carbon produced by non-photoautotrophic organisms. Starting in October 2000, the use of dark bottles was discontinued. Following practices reported in the literature (Chavez et al., 2011; Church et al., 2013), we thus calculated the mean ratio of carbon uptake in the dark and light bottles from 1989 to 2000 (5.0% ± 2%) and then used this average ratio to calculate the NPP(z) for all light bottle incubations from year 2000 onwards.

3.2.2. BATS

At BATS, samples were collected from 0 to 140 m at 20 m intervals, light and dark bottles were used throughout the time-series period. Similar to HOT, the average value of NPP in the light bottles (N = 3) was dark corrected by subtracting the value of carbon fixed in the dark bottles. The average dark bottle was found to be ~13.6% (±8%) of the light bottle (Lomas et al., 2013; Steinberg et al., 2001).

3.2.3. CARIACO

The tracer carbon uptake protocol at CARIACO is similar to that at BATS except that the samples were collected from at 1, 7, 15, 25, 35, 55, 75, and 100 m depths. More details can be found in previous studies (Lorenzoni et al., 2015; Muller-Karger et al., 2019).

3.3. Satellite data used for NPP_{model} calculations

3.3.1. Ocean color CCI datasets

NPP_{insitu} from the three time-series was further compared to NPP_{model} produced using the more recently available, long-term ocean color product, OC-CCI (v5.0) (Sathyendranath et al., 2019), which blends several existing major data streams for ocean color (starting with SeaWiFS and including MODIS, VIIRS, MERIS and OLCI) into a coherent record meeting the requirements for climate-quality products (http://www.oceancolour.org).

The 4-km resolution, 8-day OC-CCI (v5.0) data products used are: 1) *Chla*, which was generated using a blended combination of OCI, OCI2, OC2, OC3, OCx and OC5 algorithms (https://oceancolor.gsfc.nasa.gov/resources/atbd/chlor_a/; Belo Couto et al., 2016; Sathyendranath et al., 2019); 2) $a_{ph}(443)$ and $b_{bp}(443)$, which were derived using the quasi-analytical algorithm (QAA) (Lee et al., 2002), and 3) $K_d(490)$, estimated following Lee et al. (2013). All satellite products were extracted and averaged within a 3 × 3 pixel box centered at the geophysical coordinates of each NPP_{insitu} station (Bailey and Werdell, 2006).

3.3.2. PAR and SST data

Presently OC-CCI does not provide PAR and SST, we thus downloaded and used the 4-km resolution, 8-day PAR product from the GlobColour site (https://hermes.acri.fr/index.php), which is a merged product from SeaWiFS, MODIS, MERIS, OLCI and VIIRS missions. We obtained 4-km resolution, 8-day SST product of AVHRR Pathfinder Version 5.3 (PFV53) L3C dataset from NOAA National Centers for Environmental Information (NCEI) (https://doi.org/10.7289/v52j68xx).

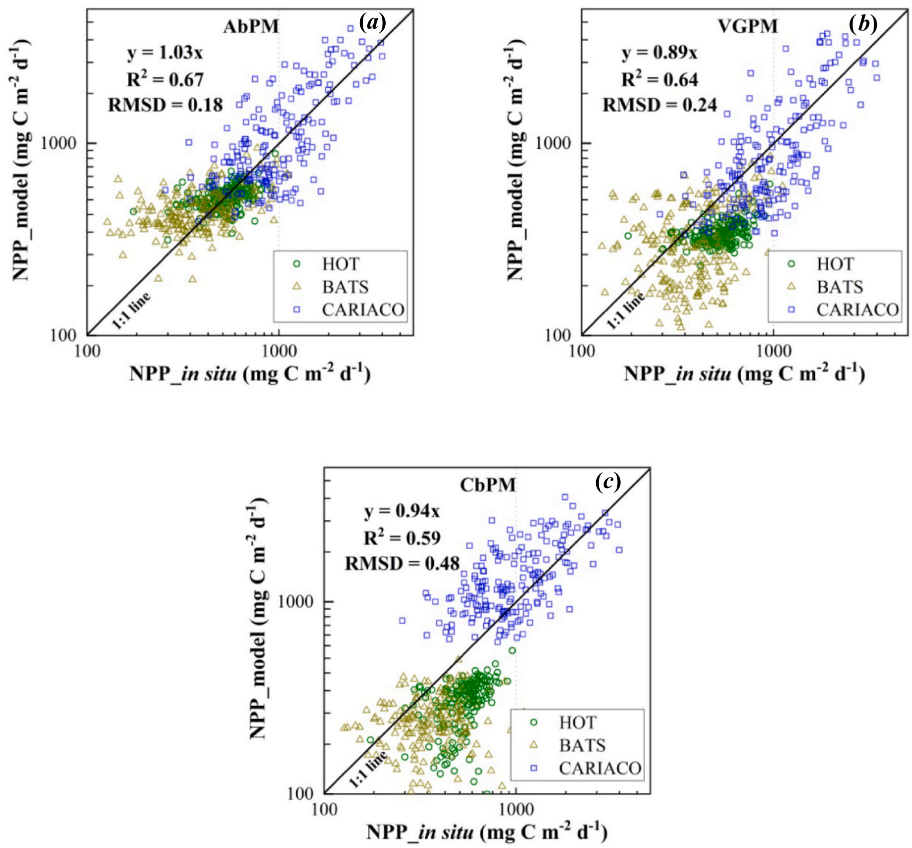

Fig. 2. Comparison between NPP_{insitu} (N = 601) from HOT (N = 188), BATS (N = 226) and CARIACO (N = 187) and NPP_{model} from (*a*) AbPM, (*b*) VGPM, and (*c*) CbPM using major inputs estimated from OC_CCI ocean color data.

Table 4
Statistical measures of comparisons between *in situ* and modeled NPP (NPP_{AbPM}, NPP_{VGPM} and NPP_{CbPM}) using OC-CCI data.

Station	Model	N	R^2	σ_d	RMSD	Bias	*u*RMSD	B*	*u*RMSD*	*u*RMSD*	cosine similarity
HOT	AbPM	188	0.33	72.4	0.10	0.00	0.10	−0.02	−0.87	0.87	0.90
	VGPM	188	0.22	48.6	0.21	−0.19	0.10	−1.64	−0.87	1.86	0.90
	CbPM	188	0.23	92.1	0.32	−0.28	0.16	−2.42	1.40	2.80	0.89
BATS	AbPM	226	0.25	117.0	0.21	0.07	0.20	0.31	−0.89	0.94	0.87
	VGPM	226	0.19	153.4	0.28	−0.10	0.26	−0.46	−1.14	1.23	0.84
	CbPM	226	0.07	105.1	0.71	−0.40	0.58	−1.78	2.57	3.13	0.71
CARIACO	AbPM	187	0.54	761.5	0.19	0.02	0.19	0.08	0.83	0.83	0.87
	VGPM	187	0.52	845.7	0.20	−0.06	0.19	−0.28	0.86	0.90	0.85
	CbPM	187	0.40	611.8	0.21	0.11	0.18	0.48	−0.81	0.94	0.86
Total	AbPM	601	0.67	546.9	0.18	0.03	0.17	0.13	−0.66	0.67	0.87
	VGPM	601	0.64	588.5	0.24	−0.11	0.21	−0.44	0.79	0.90	0.84
	CbPM	601	0.59	633.9	0.48	−0.20	0.44	−0.75	1.68	1.84	0.82

3.3.3. Climatology datasets

All the inputs required for the three models are listed in Table 2. In addition, mixed layer depths (MLD) and depths of the nitracline (Z_{NO3}) data required for CbPM were obtained as follows: MLD was obtained from the MLD climatology products generated from Hybrid Coordinate Ocean Model (HYCOM) with a resolution at 1/12° (https://www.hycom.org). Z_{NO3} was calculated from monthly climatological nutrient fields reported in the World Ocean Atlas 2013 (D'Ortenzio et al., 2014; Garcia-Corral et al., 2014) at 1° resolution and defined as the shallowest depth at which nitrate + nitrite exceed 0.5 μM (https://www.nodc.noaa.gov). All MLD and Z_{NO3} climatology data were resampled to 4-km resolution, 8-day products based on multiple interpolation methods from Software Packages (CDO, Climate Data Operators) to match the spatial and temporal resolution of the other products.

3.4. Consistency check of input satellite data

As the quality of input data is critical to the performance of the models, we first evaluated the consistency between the satellite products and *in situ* measurements. In general, input data necessary for NPP_{model}, such as *Chla*, PAR, and SST showed low bias (see Table 3) compared to *in situ* measurements (Median ratio around 1.0).

Overall, for the >300 matched datasets, satellite data products (*Chla*, PAR, and SST) showed reasonable agreement with corresponding *in situ* data from the three sites (see Table 3 and Fig. S2 in Supplementary Materials). Notice that the R^2 values of *Chla* are low at HOT and BATS sites due to some outliers and very narrow dynamic range in these subtropical oligotrophic gyres. Nonetheless, the mean ratio of *Chla* remains reasonable (0.94– 1.80) for these sites. On the other hand, satellite SST showed the highest consistency with *in situ* SST (R^2 = 0.94, MPD = 1.3%) and the lowest spread for skewed distributions as

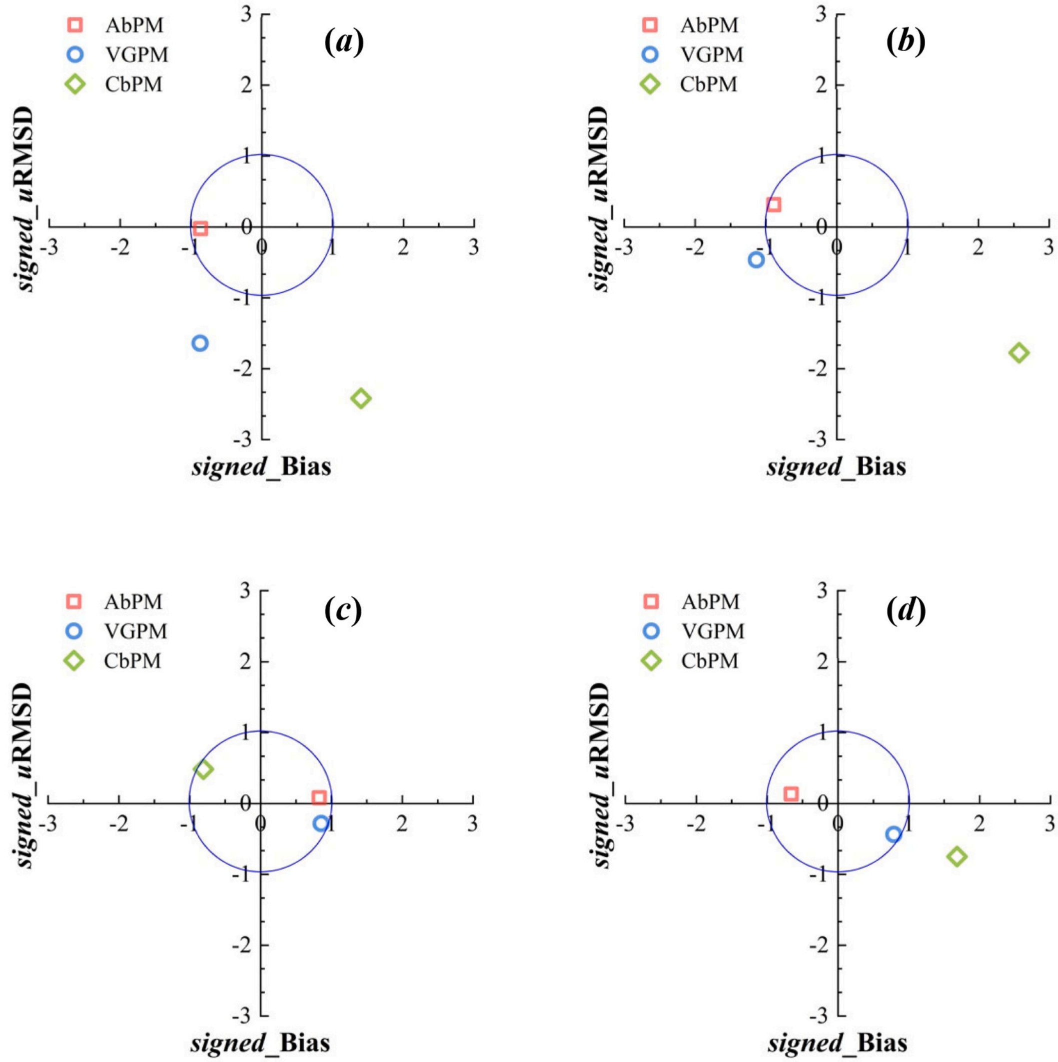

Fig. 3. Target diagram displaying Bias* (label: signed_Bias) and *u*RMSD* (label: signed_ *u*RMSD) for NPP_{model} relative to NPP_{insitu}, where the major inputs for NPP_{model} were retrieved from OC_CCI datasets. (*a*) HOT, (*b*) BATS, (*c*) CARIACO and (*d*) data from all 3 sites. The large open blue circle is the normalized standard deviation of NPP_{insitu}. The distance from the origin to each model's symbol is the RMSD* of this model. (For interpretation of the references to color in this figure legend, the reader is referred to the web version of this article.)

indicated by the low Semi Inter Quartile Range (SIQR = 0.01). Other input data for NPP_{model}, such as PAR and MLD, also showed reasonable agreement with their corresponding *in situ* values. Specifically, the R^2 values were 0.71 and 0.74, the SIQR values stood at 0.19 and 0.20, and the MPD values were 2.6% and 21.3% (see Table 3). Overall, *Chla* from ocean color satellites shows the highest uncertainty (SIQR = 0.46 and MPD = 37.2%) with the SST product presenting the lowest uncertainty (SIQR = 0.01 and MPD = 1.3%).

4. Results and discussion

4.1. Performance of NPP models

4.1.1. NPP_{model} using in situ data

In ocean color remote sensing, *Chla*, $a_{ph}(443)$ and $b_{bp}(443)$ are derived empirically, or semi-analytically, from the remote sensing reflectance spectrum (R_{rs}) of the water. Since an R_{rs} spectrum from ocean color satellites always contains various levels of uncertainties, we first compared the performance of the three NPP models using inputs (*Chla*, $a_{ph}(443)$ and $b_{bp}(443)$) calculated from *in situ* R_{rs} by algorithms described in Section 3.3.1, with resulting NPP_{model} compared with NPP_{insitu} shown in Fig. 1. For this dataset (160 points), in which NPP_{insitu} ranged from ~200–4100 mg C m $^{-2}$ d $^{-1}$, AbPM (Fig. 1*a*) performed the best with a high R^2 value (0.67), lowest RMSD (0.23) and a linear regression slope closest to unity (slope = 1.12, $P < 0.001$). This was followed by VGPM (Fig. 1*b*, $R^2 = 0.72$, RMSD = 0.46, slope = 0.70, $P < 0.001$) and then CbPM (Fig. 1*c*, $R^2 = 0.55$, RMSD = 0.41, slope = 0.68, $P < 0.001$). These results are consistent with earlier findings from other regions (Lee et al., 2011; Pinkerton et al., 2021; Song et al., 2023). All three models showed the highest correspondence (R^2) at CARIACO and the lowest at BATS. The lowest RMSD was obtained at HOT, while the highest at BATS.

Unfortunately there were limited *in situ* measurements of a_{ph} and b_{bp} at the three time-series sites, thus not possible to evaluate NPP_{AbPM} and NPP_{CbPM} using key inputs obtained *in situ*. However, there are *in situ* data of *Chla*, PAR and Z_{eu}, thus for added information, NPP_{VGPM} obtained with inputs from these *in situ* data was compared with NPP_{insitu} and shown in Fig. S3 of the Supplementary Materials. It was found that, as *Chla* from R_{rs} does not show systematic bias compared to *in situ Chla*, the outcome of NPP_{VGPM} with these inputs is similar to that with Chla estimated from *in situ* R_{rs}.

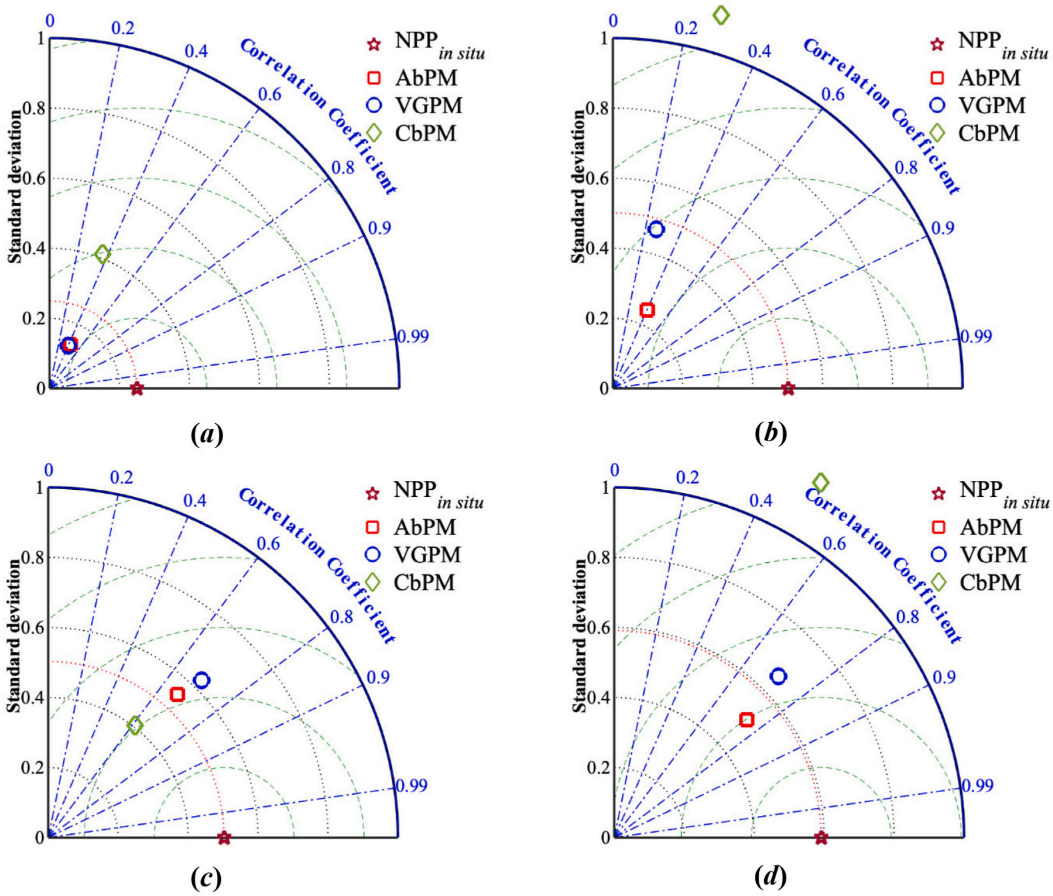

Fig. 4. Taylor diagrams of NPP_{model} from each participating model. (*a*) HOT, (*b*) BATS, (*c*) CARIACO, and (*d*) data from all 3 sites. Here the datasets are in natural logarithm format for the convenience of drawing Taylor diagrams. The distance from the origin (black dotted lines) is the standard deviation of NPP_{model}, while the red dotted line represents the standard deviation of NPP_{insitu}. The azimuth angle represents the correlation coefficient between the NPP_{insitu} and NPP_{model}, and the distance between each model symbol and NPP_{insitu} (red pentagram) is the RMSD. Green dashed lines are isolines of RMSD. Model symbols are the same as in that Fig. 3. (For interpretation of the references to color in this figure legend, the reader is referred to the web version of this article.)

4.1.2. NPP_{model} with inputs from ocean color satellites

The performance of VGPM, CbPM and AbPM was further evaluated by running these models with the OC-CCI satellite data products as primary inputs (Figs. 2*a*-c). In particular, as mentioned earlier, while all models used OC-CCI datasets, NPP_{model} from VGPM and CbPM were obtained using the model code downloaded from the Oregon State University (OSU) webpage. We characterized the performance of the three models with the following statistical measures.

A) **Regressions**: For these *in situ* and satellite matched-up time-series measurements, AbPM performed the best with the highest R^2 (0.67) and the lowest RMSD (0.18) (Fig. 2*a*), followed by VGPM (Fig. 2*b*, $R^2 = 0.64$, RMSD = 0.24) and lastly by CbPM (Fig. 2*c*, $R^2 = 0.59$, RMSD = 0.48). The better performance of AbPM is also reflected in the other statistical measures, such as slope (1.03 for AbPM, 0.89 for VGPM, 0.94 for CbPM), Bias (0.03 for AbPM, −0.11 for VGPM, −0.20 for CbPM), and *u*RMSD (0.17 for AbPM, 0.21 for VGPM, 0.44 for CbPM). Breaking down to the three sites, all three models showed the best performance at CARIACO but poor skills at BATS (see Table 4). This contrast in performance is somewhat surprising, as CARIACO is a coastal site where usually it is more challenging to estimate the bio-optical properties from satellite ocean color remote sensing. The better R^2 value at CARIACO, however, is likely mainly driven by the wide dynamic range of the data, as compared to the two oceanic sites (HOT and BATS), which have a very narrow range of *Chla* and NPP.

B) **Target diagrams**: In the Target diagrams, RMSD of NPP_{AbPM} is the model result that falls inside the large open blue circle of all sites (Fig. 3*d*), which represents the normalized standard deviation of NPP_{insitu}, while NPP_{VGPM} is close to the edge of this open blue circle and the NPP_{CbPM} is outside. This indicates that mean NPP_{AbPM} is closest to mean NPP_{insitu}. Stationwise (Figs. 3*a*-*c*), NPP_{VGPM} and NPP_{AbPM} underestimated NPP_{insitu} ($B^* < 0$) at HOT and BATS, but overestimated NPP_{insitu} ($B^* > 0$) at CARIACO, however, results of NPP_{CbPM} show the opposite. Further, NPP_{VGPM} and NPP_{CbPM} underestimated NPP_{insitu} variability ($uRMSD^* < 0$) at HOT and BATS, and NPP_{CbPM} slightly overestimated NPP_{insitu} variability ($uRMSD^* > 0$) at CARIACO, while NPP_{AbPM} shows highly consistent variability with NPP_{insitu} variability ($uRMSD^* \approx 0$) for both HOT and CARIACO, except slightly overestimated NPP_{insitu} variability ($uRMSD^* > 0$) at BATS. Overall (Fig. 3*d*), the average RMSD* (Table 4) of NPP_{AbPM} *vs* average RMSD* of NPP_{insitu} for data from all three sites was as low as 0.67, followed by NPP_{VGPM} (0.90) and NPP_{CbPM} (1.84), which indicated that AbPM shows lower forecasting errors and more accuracy in predictions.

C) **Taylor diagrams:** Taylor diagrams (Taylor, 2001) complement Target diagrams by providing additional information pertaining to the difference in variability associated with modeled *vs.* observed values. In the Taylor diagrams (Figs. 4*a*-*d*), the standard deviation (SD_{Ln}), the Pearson's correlation coefficient (r_{Ln}) and the root mean square difference ($RMSD_{Ln}$) between $Ln(NPP_{model})$ and $Ln(NPP_{insitu})$ (here the datasets are in natural logarithm

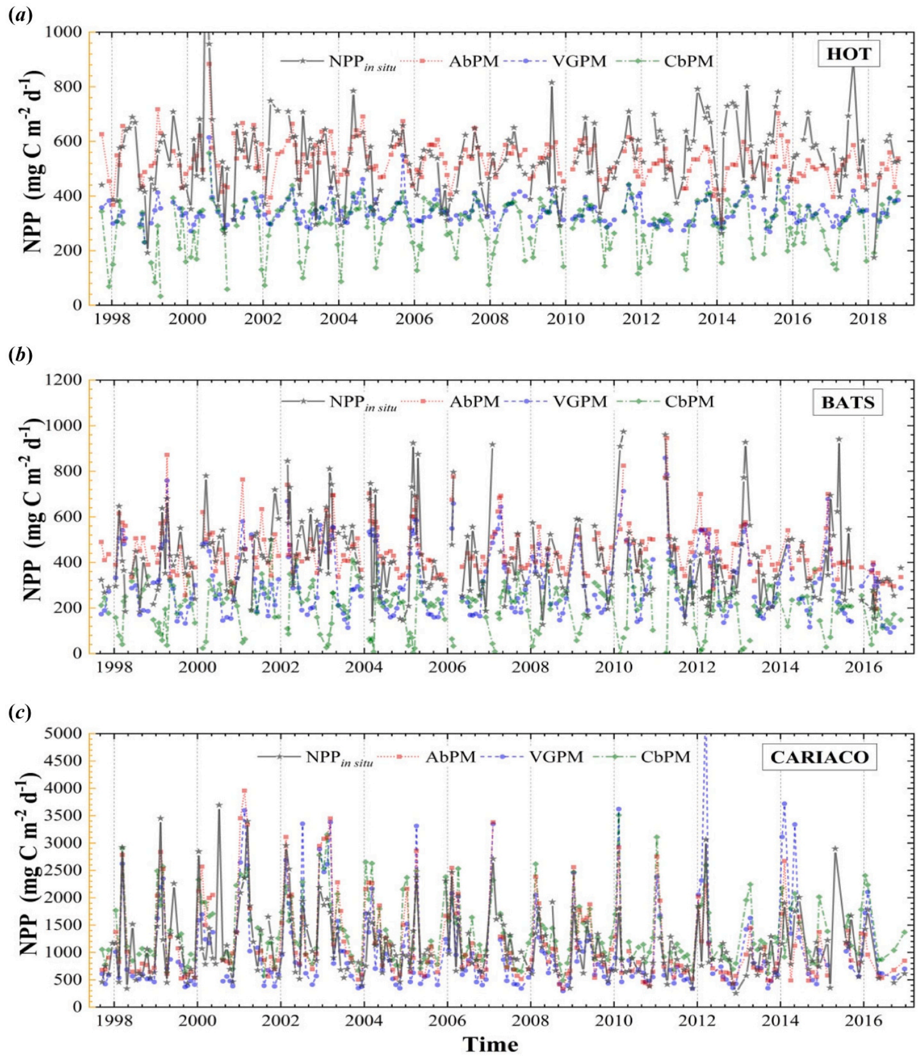

Fig. 5. Time-series of NPP$_{insitu}$, NPP$_{AbPM}$, NPP$_{VGPM}$, and NPP$_{CbPM}$. (*a*) HOT, (*b*) BATS, and (*c*) CARIACO.

format for the convenience of drawing Taylor diagrams) are displayed together to provide a visual evaluation of the performance of each model. Note that a model performs better if its symbol falls closer to the reference point (red pentagram) where r_{Ln} is 1.0, which also represents the magnitude of NPP$_{insitu}$ variance. Overall (see Fig. 4*d*), the SD$_{Ln}$ of NPP$_{model}$ from all three sites ranged from 0.51 (NPP$_{AbPM}$) to 1.17 (NPP$_{CbPM}$). The Taylor diagram showed that r_{Ln} mostly ranged between 0.50 and 0.75. It is noteworthy that, when putting data of all three sites together, both NPP$_{AbPM}$ and NPP$_{VGPM}$ reproduced the magnitude of NPP$_{insitu}$ variance (SD$_{Ln}$ = 0.59), but not NPP$_{CbPM}$. At HOT (Fig. 4*a*), all three models have similar r_{Ln} ($\sim$ 0.4) with NPP$_{insitu}$. At BATS (Fig. 4*b*), both NPP$_{CbPM}$ and NPP$_{VGPM}$ had lower r_{Ln} values (< 0.3), while NPP$_{AbPM}$ was comparatively better (r_{Ln} = 0.4). NPP$_{VGPM}$ showed slight underestimates but the closest SD$_{Ln}$ of NPP$_{insitu}$. The low NPP$_{insitu}$ variance for HOT (SD$_{Ln}$ = 0.25) and for BATS (SD$_{Ln}$ = 0.50) can be attributed to the perennial oligotrophy of these waters. NPP$_{AbPM}$ produced slightly lower values compared to NPP$_{insitu}$, and exhibited highest consistency in r_{Ln} of NPP$_{insitu}$, whereas both NPP$_{VGPM}$ and NPP$_{CbPM}$ notably underestimated NPP$_{insitu}$ values and displayed insufficient consistency in the r_{Ln} of NPP$_{insitu}$ in HOT and BATS. Coastal CARIACO time-series station showed the highest r_{Ln} (0.61– 0.73) for all models, with NPP$_{AbPM}$ showing the highest r_{Ln} (0.73), along with its SD$_{Ln}$ (0.55) approximating the SD$_{Ln}$ of NPP$_{insitu}$ (0.50). All the above statistical measures show that AbPM yielded values of NPP that were more consistent in magnitude and variance than those obtained using VGPM and CbPM.

4.2. Long-term monthly time-series of NPP

Figs. 5*a*-c show the long-term ($\sim$20 years, from September 1997 to $\sim$2017) time-series of NPP$_{insitu}$ and NPP$_{model}$ estimates at *a*) HOT, *b*) BATS and *c*) CARIACO. The plots show the seasonal cycles and the considerable interannual variations in NPP.

At HOT (Fig. 5*a*), NPP$_{AbPM}$ closely tracked NPP$_{insitu}$, especially the clearly defined summer peaks and the inter-annual variability, except for the slighly lower values than NPP$_{insitu}$ during the period 2012–2017. Peak values of NPP$_{insitu}$ (541.4 $\pm$ 87.6 mg C m $^{-2}$ d $^{-1}$) matched those from NPP$_{AbPM}$ (528.5 $\pm$ 47.4 mg C m $^{-2}$ d $^{-1}$) very well. NPP$_{VGPM}$ consistently exhibited lower values compared to NPP$_{insitu}$, with no apparent monthly or seasonal fluctuations observed. NPP$_{CbPM}$ similarly underestimated NPP$_{insitu}$, however, it frequently displayed peaks during early spring. These differences in the timing of NPP peaks was also reported by other researchers (Ma et al., 2014; Westberry et al., 2008). Of the three models, AbPM modeled best the high NPP due to summer blooms at the HOT station and most accurately displayed the seasonal cycles observed in NPP$_{insitu}$.

The seasonal variability of NPP$_{insitu}$ at BATS (Fig. 5*b*) was more pronounced, and in general, both NPP$_{AbPM}$ and NPP$_{VGPM}$ were able to

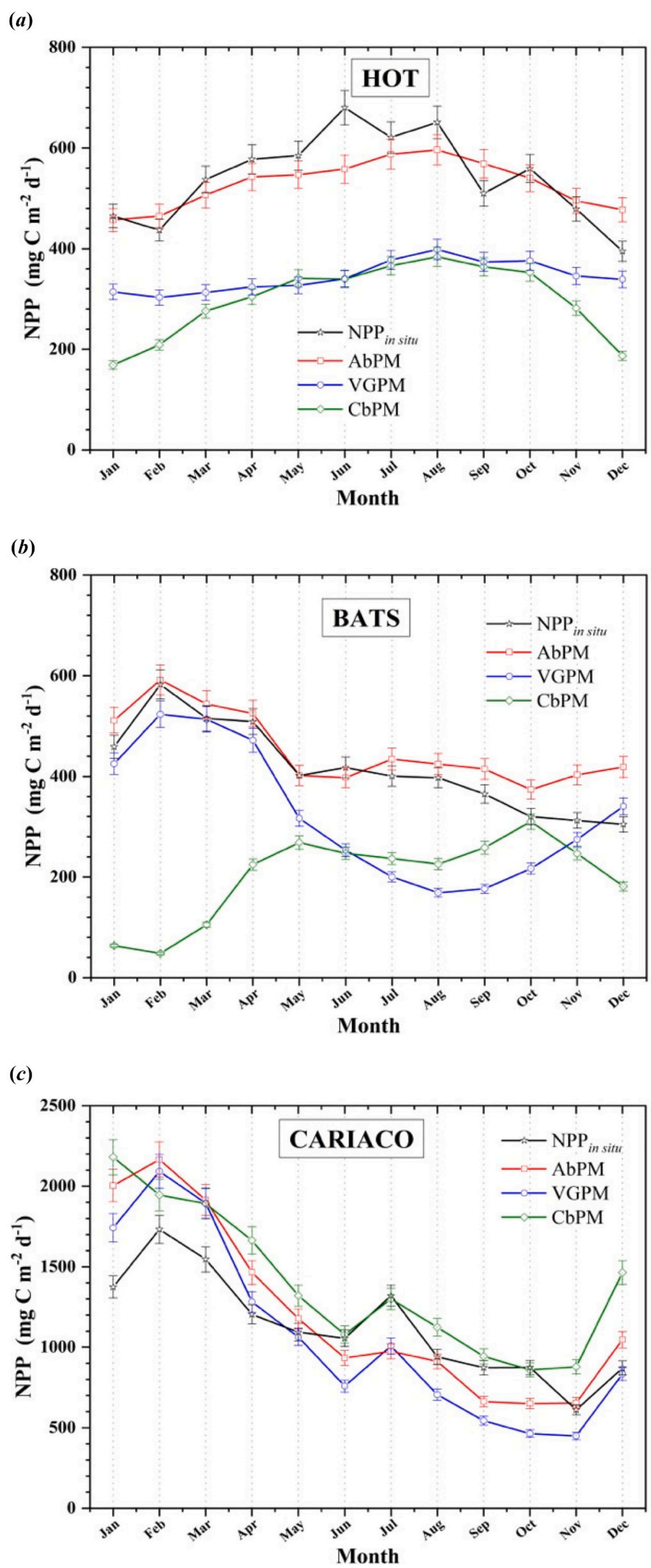

Fig. 6. Monthly climatology from NPP_{insitu}, NPP_{AbPM}, NPP_{VGPM}, and NPP_{CbPM}. (*a*) HOT, (*b*) BATS, and (*c*) CARIACO. The error bar is the 95% confidence level.

capture the spring peaks, but not NPP_{CbPM}. The seasonal minimum of NPP_{CbPM} (~ 48 mg C m $^{-2}$ d $^{-1}$) was about six fold lower than the seasonal minimum of NPP_{insitu} (~ 304 mg C m $^{-2}$ d $^{-1}$) and often, these minima seen in NPP_{CbPM} aligned more closely with water column *Chla*, which was also indicated in Westberry et al. (2008).

At CARIACO, all three models were able to capture the pronounced seasonal cycle and interannual variations in NPP_{insitu} (Fig. 5*c*). Again, the best fit was provided by NPP_{AbPM}. Moreover, of importance is that NPP_{AbPM} captured the significantly reduced NPP_{insitu} peaks in 2008–2011 and 2013– 2016.

In summary, it is clear that NPP_{AbPM} not only performed better in capturing the magnitude of NPP_{insitu}, but it also reproduced the seasonal cycles of NPP_{insitu} much better than the other two models.

4.3. Monthly climatology of NPP

The monthly climatology of NPP_{insitu} and NPP_{model} at the three sites was calculated using the 20+ year time-series (Figs. 6*a*-c, Table 5). At HOT, the monthly climatology of NPP_{insitu} showed weak monthly variations in spring (March to May), with NPP_{insitu} peaking in summer with a high around 620 mg C m $^{-2}$ d $^{-1}$. This monthly climatology is well captured by NPP_{AbPM} (Fig. 6*a*). We noticed the not-exact match in the temporal shape between NPP_{AbPM} and NPP_{insitu}, but the two temporal variations of NPP_{AbPM} and NPP_{insitu} actually agree with each other very well if the interannual variability of each is considered. Both NPP_{VGPM} and NPP_{CbPM} showed weak seasonal variations in NPP, and the NPP values were about a factor of 1.6 (for NPP_{VGPM}) and 1.9 (for NPP_{CbPM}) lower than NPP_{insitu}. On the other hand, NPP_{CbPM} obtained significantly lower NPP for winter months, which could also be clearly observed in the time-series (Fig. 5*a*).

At BATS (Fig. 6*b*), NPP_{AbPM} mirrored the monthly trend of NPP_{insitu} averaging ~585.0 mg C m $^{-2}$ d $^{-1}$ for the Jan.-Apr. period, while a climatology minimum in August shown by NPP_{VGPM} was not observed either in NPP_{insitu} or in NPP_{AbPM}. In contrast, it appears that NPP_{CbPM} showed opposing monthly variations compared to NPP_{insitu} and that from other models, suggesting serious uncertainties in NPP_{CbPM} for this region.

Being a continental shelf station influenced by upwelling, NPP_{insitu} at the CARIACO was much higher and displayed a more pronounced seasonality than that at HOT and BATS (Fig. 6*c*). NPP_{insitu} peaked in Feb. with the highest value ~1493.8 mg C m $^{-2}$ d $^{-1}$, then steadily decreased to a low ~662.7 mg C m $^{-2}$ d $^{-1}$ in Nov.-Dec., with a secondary peak in July. It appears that all three models captured this pattern very well, except that CbPM overestimated NPP in winter and failed to reproduce the seasonal peak in Feb. seen in NPP_{insitu}.

The above analysis clearly shows that at all three sites (Table 5), AbPM could capture not only the seasonal cycle but the magnitude of variability as well, a performance not observed for VGPM and CbPM. Further, VGPM performed better than CbPM for the three sites.

4.4. Observed interannual trends in NPP

4.4.1. HOT

For the period between 1988 and 2018, the yearly average from daily NPP_{insitu} at HOT remained relatively constant with a mean around 539.1 (± 125.2) mg C m^{-2} d^{-1}. This constancy is also reflected in the NPP_{model} products (see Fig. 7*a*), but the NPP_{VGPM} and NPP_{CbPM} values were systematically lower over the entire time-series (Table 6). The lower NPP_{VGPM} is completely opposite to that observed by Shih et al. (2021) for a time-series in the South China Sea, where they found that NPP_{VGPM} was ~50% higher than NPP_{insitu}.

The trend in the ~20-year-long NPP_{insitu} time-series dataset suggests a weak increasing trend of the order +4.1 mg C m^{-2} d^{-1} per year ($P < 0.01$) from 1988 onwards to 2018, a finding consistent with other recent reports (Gregg and Rousseaux, 2019; Karl et al., 2021). This increasing trend weakens to +2.3 mg C m^{-2} d^{-1} per year ($P < 0.05$) when the duration is limited to 1997–2018. This "increase", however, is apparently driven more by the low values (~450 mg C m^{-2} d^{-1}) of 1997–1998 *vs* the high values (~550 mg C m^{-2} d^{-1}) of 2014–2015 as is evident from the lack of an obvious trend (+0.68 mg C m^{-2} d^{-1} per year) for the period between 2000 and 2018, as reported earlier (Chavez et al., 2011;

Table 5
Statistical measures (R^2 and RMSD) between *in situ* and modeled NPP (NPP_{AbPM}, NPP_{VGPM} and NPP_{CbPM}) using OC-CCI data for monthly climatology and yearly average values.

Station	Model	Monthly climatology			Model	Yearly averages		
		N	R^2	RMSD		N	R^2	RMSD
	AbPM	12	0.71	0.04	AbPM	22	0.22	0.05
HOT	VGPM	12	0.21	0.20	VGPM	22	0.05	0.20
	CbPM	12	0.66	0.28	CbPM	22	0.08	0.27
	AbPM	12	0.83	0.06	AbPM	20	0.33	0.08
BATS	VGPM	12	0.59	0.19	VGPM	20	0.21	0.14
	CbPM	12	0.49	0.48	CbPM	20	0.03	0.32
	AbPM	12	0.80	0.10	AbPM	20	0.53	0.07
CARIACO	VGPM	12	0.88	0.13	VGPM	20	0.36	0.09
	CbPM	12	0.69	0.12	CbPM	20	0.33	0.12

Church et al., 2013; Hirawake et al., 2011; Koslow and Allen, 2011; Saba et al., 2010). Previous studies based on NPP_{insitu} have reported a significant decreasing trend (-6.6 mg C m^{-2} d^{-1} per year, $P < 0.01$) from 2000 to 2010, followed by an increasing trend ($+9.3$ mg C m^{-2} d^{-1} per year, $P < 0.01$) until 2015 after which NPP_{insitu} decreased (Boyce et al., 2010; Krumhardt et al., 2017; Kulk et al., 2020). Assessing the robustness of these trends for climate studies will clearly require a time-series of longer lengths.

Of the three models, it is evident that only NPP_{AbPM} most closely tracked the interannual variations observed in NPP_{insitu} (Figs. 5*a*, 7*a*), although NPP_{AbPM} deviated from NPP_{insitu} to some extent after 2012. There have been many studies discussing the various reasons regarding the difference between satellite estimates and *in situ* measurements (Gregg and Rousseaux, 2019; Karl et al., 2021; Kavanaugh et al., 2018) as was observed post 2012. For instance, there could be uncharacterized geographic variability (Kavanaugh et al., 2018), or a potential shift in phytoplankton communities (Gregg and Rousseaux, 2019). More specifically, Karl et al. (2021) observed that the increase in NPP_{insitu} at HOT is not uniform throughout the water column, whereas NPP_{model} is biased towards the light-saturated layer. All of these emphasize the importance of depth-resolved NPP (Brewin et al., 2021; Sathyendranath et al., 2020) and the necessity of using phytoplankton community specific photosynthetic parameters in NPP algorithms (Wu et al., 2022). The other two models didn't capture the magnitude, seasonal amplitude and interannual changes in NPP_{insitu} at HOT (Fig. 7*a*).

4.4.2. BATS

Daily NPP_{insitu} at BATS averaged 419.9 ($\pm$ 194.4) mg C m^{-2} d^{-1} and significant ($P < 0.05$) interannual variations were observed (Figs. 5*b*, 7*b*). Of the three time-series stations, BATS showed the most prominent changing trends in the annual NPP_{insitu}. From 1997 to 2016, NPP_{insitu} at BATS generally declined at an average rate of about -2.2 mg C m^{-2} d^{-1} per year (Table 6), with the greatest decline (-9.3 mg C m^{-2} d^{-1} per year, $P < 0.01$) between 2008 and 2016. This significant decreasing trend observed over our study period is similar to -5.6 mg C m^{-2} d^{-1} per year during the 1990–2016 period reported by D'Alelio et al. (2020). What is noteworthy, however, is the trends of increasing NPP_{insitu} ($+7.9$ mg C m^{-2} d^{-1} per year, $P < 0.01$) during 1997 to 2007 in our research, which was reported a decade ago by Saba et al. (2010), who observed that during the period between 1989 and 2007, NPP_{insitu} at BATS had increased by an average of nearly 2% per year, a result consistent with other studies for the same period (Chavez et al., 2011; Church et al., 2013; Hirawake et al., 2011). However, a following study (Lomas et al., 2013) found a slow but significant decline in NPP_{insitu} from 1988 to 2012 associated with a decline in total microplankton and a slow increase in prokaryote contribution to NPP over time. Both studies (D'Alelio et al., 2020; Lomas et al., 2013) have suggested that this long-term shift in the ecosystem should have a significant impact on the carbon cycle at BATS. The declining trends reported by us (Table 6) are consistent with Lomas et al. (2013), and could be the result of the biogeochemical transition at BATS beginning in the mid-2000s (Figs. 5*b*, 7*b*), possibly due to a shift in phytoplankton community composition (Krause et al., 2009; Lomas et al., 2022).

AbPM and CbPM obtained the correct trending sign of the NPP_{insitu} during 2007–2016 at BATS, but VGPM shows no trend (Table 6). On the other hand, for trends before 2007, both AbPM and VGPM got the same sign as that (increase) observed with NPP_{insitu}, but not CbPM. Further, none of the three models captured the transition of NPP_{insitu} trends in the mid-2000s, although they provided the more recent downward trend of NPP_{insitu}. As for the many peaks and troughs observed in NPP_{insitu}, none of the models captured them very well, while these models reproduced the increase of NPP_{insitu} in 2010 and 2015 corresponding to strong/very strong El Niño (warm) events. AbPM, in summary, most accurately replicates these interannual trends.

4.4.3. CARIACO

Interannual variations (1112.4 $\pm$ 609.8 mg C m^{-2} d^{-1}) in annual NPP_{insitu} were most pronounced at CARIACO. Significant ($P < 0.01$) changes in NPP_{insitu} were observed (Figs. 5*c*, 7*c*), with a declining rate of -8.5 mg C m^{-2} d^{-1} per year for the period between 1997 and 2016. We detected strong oscillations at this station over the two-decade time-series. The slope of NPP series *versus* time is no longer close to zero as was reported earlier by Chavez et al. (2011), nor has it decreased. Instead, trends in NPP_{insitu} reveal a gradual decrease (-18.3 mg C m^{-2} d^{-1} per year, $P < 0.01$) after 2003 (Figs. 5*c*, 7*c*), similar to more recent findings (Church et al., 2013; Muller-Karger et al., 2019), who attributed this decline in NPP to weakening of upwelling after 2003 in response to weakened trade winds and warming of the Atlantic. All models also displayed a significant increasing trend before 2003 (Table 6), with NPP_{AbPM} performing better than the others in tracking NPP_{insitu}. Only NPP_{AbPM} successfully captures the decreasing trend of NPP_{insitu} after 2003 and between 1997 and 2016.

4.4.4. Summary of in situ and NPP model-derived climatologies and trends at three time-series stations

The increase in NPP at HOT and the decreases observed at BATS and CARIACO indicate that NPP is sensitive to changes in plankton community structure and/or to interannual variations in hydrographic forcing or basin-scale climate fluctuations (Church et al., 2013; Ducklow et al., 2009; Karl et al., 2021; Lomas et al., 2013; Muller-Karger et al., 2019). Among the three contrasting models studied here (see Tables 5 and 6), AbPM clearly showed better capabilities in capturing the seasonality, monthly climatologies and interannual variability observed in NPP_{insitu}. It is worth mentioning that some discrepancies between trends in NPP and those in earlier literature might arise from the fact that our time period of the analysis is longer than those in earlier reports. However, we could reproduce the trends reported by Saba et al. (2010) and Chavez et al. (2011) for HOT and BATS when we restricted our analysis to the period (1997–2004 and 1997–2007) reported in their studies. Additionally, as in previous studies, end-point bias correction was applied to estimate trends, which can prevent anomalous data at the beginning or end of a time-series from overly influencing the detection

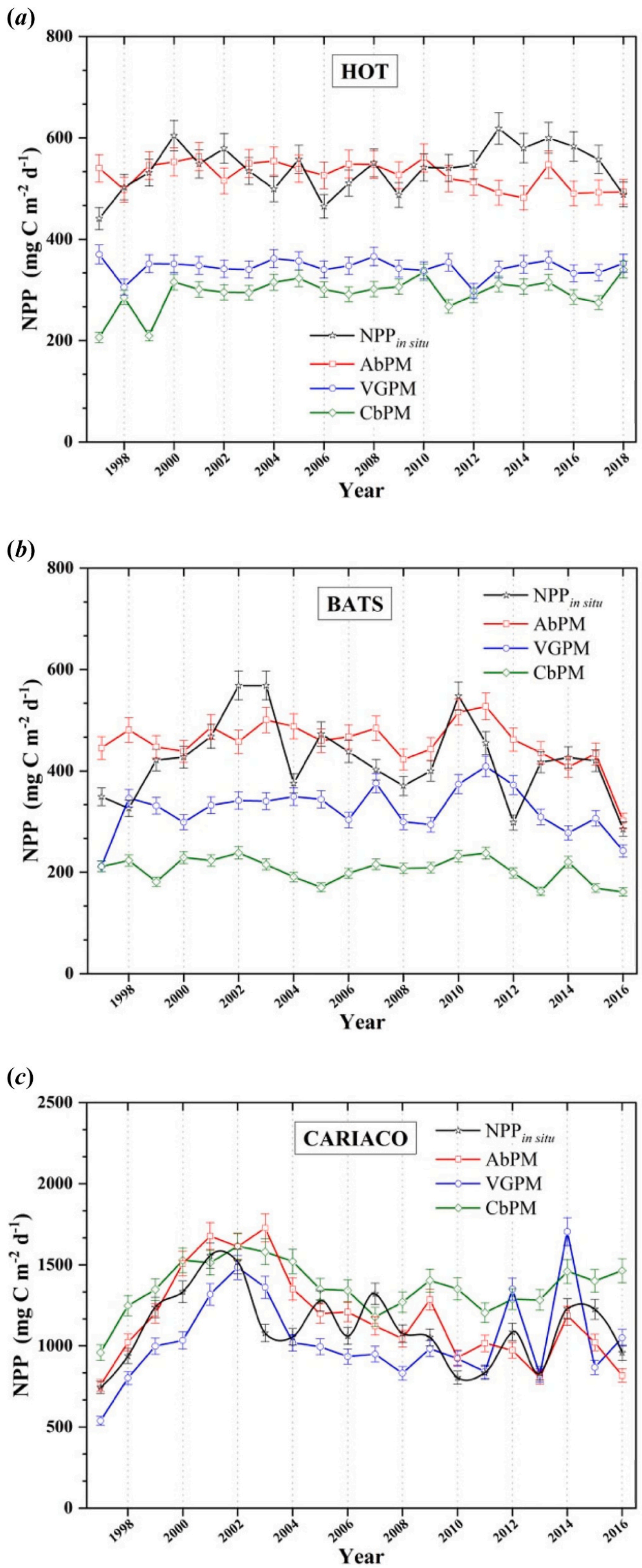

Fig. 7. Yearly averages of daily NPP$_{insitu}$, NPP$_{\text{AbPM}}$, NPP$_{\text{VGPM}}$, and NPP$_{\text{CbPM}}$. (*a*) HOT, (*b*) BATS, and (*c*) CARIACO stations. The error bar is the 95% confidence level.

of a trend (Rousseaux and Gregg, 2015).

Due to large fluctuations in annual NPP$_{insitu}$ and the corresponding NPP$_{\text{model}}$, trends assessments are affected by the time period of the study, where different trends can emerge when data from different periods are analyzed (Lee et al., 2010). For the purpose of this study, we focused on examining if the models were able to capture the seasonal and interannual variations observed in NPP$_{insitu}$. Towards this end, we employed cosine similarity between *in situ* and modeled annual NPP time series to gauge their closeness (see Table 4), as cosine similarity is a measure of similarity between two sequences of numbers (a value of 1.0 indicates completely match). This analysis shows that of the three models tested, AbPM best captures the annual variation in NPP$_{insitu}$ for the total data (0.87) as well as at each site (0.90 at HOT, 0.87 at BATS and 0.87 at CARIACO), followed by VGPM and CbPM with 0.84 and 0.82, respectively, for the total data.

Another point worth noting is that episodic large-scale climatic events, such as the El Niño–Southern Oscillation (ENSO), North Atlantic Oscillation (NAO), *etc.*, can influence NPP. To facilitate this evaluation, we have introduced Table S1, summarizing statistics on the correlation between NPP from *in situ* measurements and models at three sites, in relation to seven climate indices. The results reveal significant correlations between the variation in NPP$_{insitu}$ and SST changes associated with changes in the climatic indices. However, the degree of influence varies across different climate indices for each site. Specifically, NPP at HOT exhibits significant correlations with Multivariate El Niño-Southern Oscillation Index (MEI) and NAO, NPP at BATS is closely linked with Trans-Niño Index (TNI), and NPP at CARIACO is dominated by the Pacific Decadal Oscillation (PDO) and NAO. This analysis opens avenues for further exploration and research in understanding the varying impacts of different climate indices on seasonal to decadal fluctions in NPP at these three long-time series sites.

4.5. Empirical Cumulative Distribution Function (ECDF) of NPP

The ECDF described in section 2.4 allows for a comparison between the range and median monthly NPP$_{insitu}$ *versus* that of NPP$_{\text{model}}$ from the three models (Fig. 8). The first quartile (Q_1), median (m) and third quartile (Q_3) are typically represented as the point (unit: mg C m^{-2} d^{-1}) on the cumulative distribution curve where the curve crosses the 0.25, 0.5 and 0.75 probability level. At HOT, AbPM ($Q_1 = 480.5$, $m = 520.3$, $Q_3 = 570.3$) reproduced the range ($Q_1 = 461.6$, $Q_3 = 618.0$) and median ($m = 545.6$) of the entire NPP$_{insitu}$ dataset very well, but VGPM ($Q_1 = 311.1$, $m = 336.5$, $Q_3 = 366.6$) and CbPM ($Q_1 = 244.4$, $m = 316.9$, $Q_3 = 360.0$) underestimated both. At BATS, the ECDF of NPP$_{insitu}$ ($Q_1 = 279.2$, $m = 397.2$, $Q_3 = 515.0$) best matched with that of NPP$_{\text{AbPM}}$ ($Q_1 = 377.2$, $m = 433.9$, $Q_3 = 515.8$) values above the median, while in case of NPP$_{\text{VGPM}}$ ($Q_1 = 198.0$, $m = 296.3$, $Q_3 = 460.9$) for values below the median. Both NPP$_{\text{AbPM}}$ and NPP$_{\text{VGPM}}$ reproduced ranges similar to that of NPP$_{insitu}$, but no NPP$_{\text{CbPM}}$ ($Q_1 = 130.5$, $m = 217.4$, $Q_3 = 268.9$). At CARIACO, all three models reproduced the range and median values of NPP$_{insitu}$, with NPP$_{\text{AbPM}}$ ($Q_1 = 654.4$, $m = 917.9$, $Q_3 = 1536.8$) showing an almost exact ECDF as that for the *in situ* data ($Q_1 = 671.6$, $m = 925.9$, $Q_3 = 1350.1$), with VGPM ($Q_1 = 515.0$, $m = 730.5$, $Q_3 = 1240.1$) and CbPM ($Q_1 = 901.4$, $m = 1173.4$, $Q_3 = 1735.6$) followed. In summary, when the ECDF results of the three sites are taken together, it is apparent that AbPM could reproduce the range and median of the whole NPP$_{insitu}$ datasets very well for the three sites, while VGPM and CbPM could also do so successfully at CARIACO, but both models significantly underestimated NPP at the other two sites.

5. Brief discussion of the three NPP models

As discussed in earlier studies (Lee et al., 2015b; Saba et al., 2011) and shown here, NPP$_{\text{model}}$ results from satellite ocean color measurements are highly dependent on the NPP model used. While it is impossible to compare and evaluate all published NPP models (Campbell et al., 2002; Carr et al., 2006; Saba et al., 2011), our study focused on three fundamentally contrasting models that are representative of the two

Table 6
Interannual trend (in mg C m^{-2} d^{-1} $year^{-1}$) over different time intervals, along with the *p*-values and statistical mean (standard deviation) of *in situ* and modeled NPP (NPP_{AbPM}, NPP_{VGPM} and NPP_{CbPM}) using OC-CCI data.

Station	NPP Source	Mean NPP	*Overall Trend*	Entire Period	Period 1	Period 2
		mg C m^{-2} d^{-1}		*1997–2018*	*2000–2010*	*2010–2018*
HOT	NPP_{insitu}	539 ± 125	Increasing	+2.3*	−6.6**	−1.9*
	AbPM	526 ± 73	Decreasing	−1.8*	−0.4	−5.6**
	VGPM	343 ± 49	No Trend	−0.4	−0.2	+1.4
	CbPM	301 ± 90	Increasing	+2.2*	+1.1*	+0.6*
				1997–2016	*1997–2007*	*2007–2016*
BATS	NPP_{insitu}	420 ± 194	Decreasing	−2.2*	+7.9**	−9.3**
	AbPM	458 ± 117	Decreasing	−3.1*	+2.6*	−13.7**
	VGPM	331 ± 153	No Trend	+0.1	+7.2**	−8.0**
	CbPM	203 ± 105	Decreasing	−1.6*	−1.79*	−6.8**
				1997–2016	*1997–2002*	*2002–2016*
CARIACO	NPP_{insitu}	1112 ± 610	Decreasing	−8.5**	+166.5**	−18.3**
	AbPM	1221 ± 761	Decreasing	−20.9**	+187.1**	−30.5**
	VGPM	1078 ± 850	Increasing	+7.1**	+180.6**	+4.0*
	CbPM	1396 ± 599	Increasing	+1.5*	+121.6**	−4.3*

* *$P < 0.05$.*
** *$P < 0.01$.*

strategies employed, *i.e.*, biomass-based (*Chla* and C_{phy}) and absorption-based (a_{ph}) NPP models. As articulated in Lee et al. (2015b), each strategy/model has its own advantages and challenges, but overall a_{ph}-based or AbPM has fewer or no parameters that are tangled between photosynthesis and optical properties and hence is less beleaguered by uncertainties from model inputs, at least in principle (Westberry et al., 2023).

More specifically, for VGPM, the uncertainties arise from both *Chla* estimated from ocean color measurements and P^{B}_{opt} estimated empirically based on SST. In the case of the latter parameter, Behrenfeld et al. (2005) concluded that "a clear path for globally modeling or remotely observing variability in chlorophyll-specific photosynthesis has even to this day never been identified". As highlighted in Lee et al. (2015b) and Lee and Marra (2022), a strategic limitation of Chl-based NPP models, including VGPM, is the implicit and independent involvement of phytoplankton-specific absorption coefficient (a^{*}_{ph}) in the remotely sensed *Chla* and in P^{B}_{opt}, where compound errors will be introduced when inconsistent a^{*}_{ph} are embedded in these parameters (Lee et al., 2015b; Lee and Marra, 2022).

CbPM is more complex than VGPM, and it avoids the association of a^{*}_{ph}, thus a better estimation of NPP from remote sensing is assumed. However, phytoplankton carbon (C_{phy}) at present is empirically estimated from $b_{bp}(443)$, where large deviations exist between carbon and $b_{bp}(443)$ even in field measurements (Loisel et al., 2007; Stramski et al., 2008). Further, when $b_{bp}(443)$ is inverted from ocean color measurements, it represents a bulk optical property that may include various levels of contributions from inorganic particles, detritus and bubbles (Randolph et al., 2014; Stramski et al., 2004; Zhang et al., 1998). In addition, as NPP is converted from C_{phy} by introducing the phytoplankton growth rate, which is parameterized using the ratio of *Chla*/C_{phy}, another set of uncertainties will be introduced. Our results are consistent with the current understanding that efforts to combine more sophisticated satellite products with improved Chl-based and Carbon-based models have only slightly improved NPP accuracy (Kahru, 2017) and none of these algorithms perform exceptionally well when validated against *in situ* NPP measurements (Regaudie-de-Gioux et al., 2019).

AbPM by design avoids the involvement of a^{*}_{ph}, thus better results have been achieved as demonstrated in the literature (Lee et al., 1996; Lee et al., 2011; Marra et al., 2003), which are further reflected in the time-series comparisons presented here and in other studies (Song et al., 2023). While a_{ph}, an optical property, can be analytically or semi-analytically derived from an ocean color spectrum, the required quantum yield of phytoplankton photosynthesis (ϕ) has to be estimated or modeled (Ma et al., 2014; Zoffoli et al., 2018). If the estimation of this parameter can be further improved for the global ocean, more accurate NPP products from satellite ocean color measurements are achievable. For instance, Wu et al. (2022) recently scaled limited ϕ measurements obtained from a single cruise in the complex waters surrounding the Korean Peninsula using a coupled bio-optical-hydrographic province partitioning scheme called BIOMES. NPP_{model} generated using this approach agreed extremely well with *in situ* measurements when AbPM was applied to ocean color data provided 8 times a day by the Korean Geostationary Ocean Color Imager (GOCI). In short, while there is still room to improve the derivation of a_{ph} from satellite ocean color measurements, further improvements in global AbPM-derived NPP will depend immensely on robust ways to scale limited shipboard measurements of ϕ across different biogeochemical provinces (Lee et al., 2015b; Lee and Marra, 2022).

6. Conclusions

In this study, we assessed the performance of three contrasting NPP models by examining their ability to estimate the magnitude, variability, and trends observed in NPP_{insitu} at three long-term time-series sites, two of which (HOT and BATS) were located in oligotrophic ocean waters and one in a coastal upwelling eutrophic basin (CARIACO). NPP_{insitu} data, which span over two decades from these three long time-series stations, provided us the basis for a better understanding of uncertainties in different satellite-based NPP products, the associated discrepancies in trends with different models, and the need for robust estimates of NPP for global carbon cycling and long-term climate change studies.

Of the three models used for estimating NPP, AbPM provided the most consistent NPP compared to NPP_{insitu} in magnitudes and trends. The two other widely-used models, VGPM and CbPM, underestimated NPP in the oligotrophic waters of HOT and BATS. At BATS, the wide range of interannual variations of NPP_{insitu} were not well reproduced by these models, indicating either difficulites of these models for such an ecosystem or limitations of comparisons between satellite data and *in situ* measurements. The downtrends of NPP_{insitu} at CARIACO were discernible from all NPP models, but AbPM provided the most accurate estimates of NPP among the models evaluated for the entire period (1997–2016). Overall, the results from this study point towards AbPM as a more suitable approach towards obtaining robust NPP estimates from satellite ocean color measurements, especially because of its superior ability to capture the temporal variations observed in field NPP measurements. Further improvements in the AbPM-derived NPP values are possible with better methods to parameterize and scale-up limited field measurements of quantum yield of phytoplankton photosynthesis to

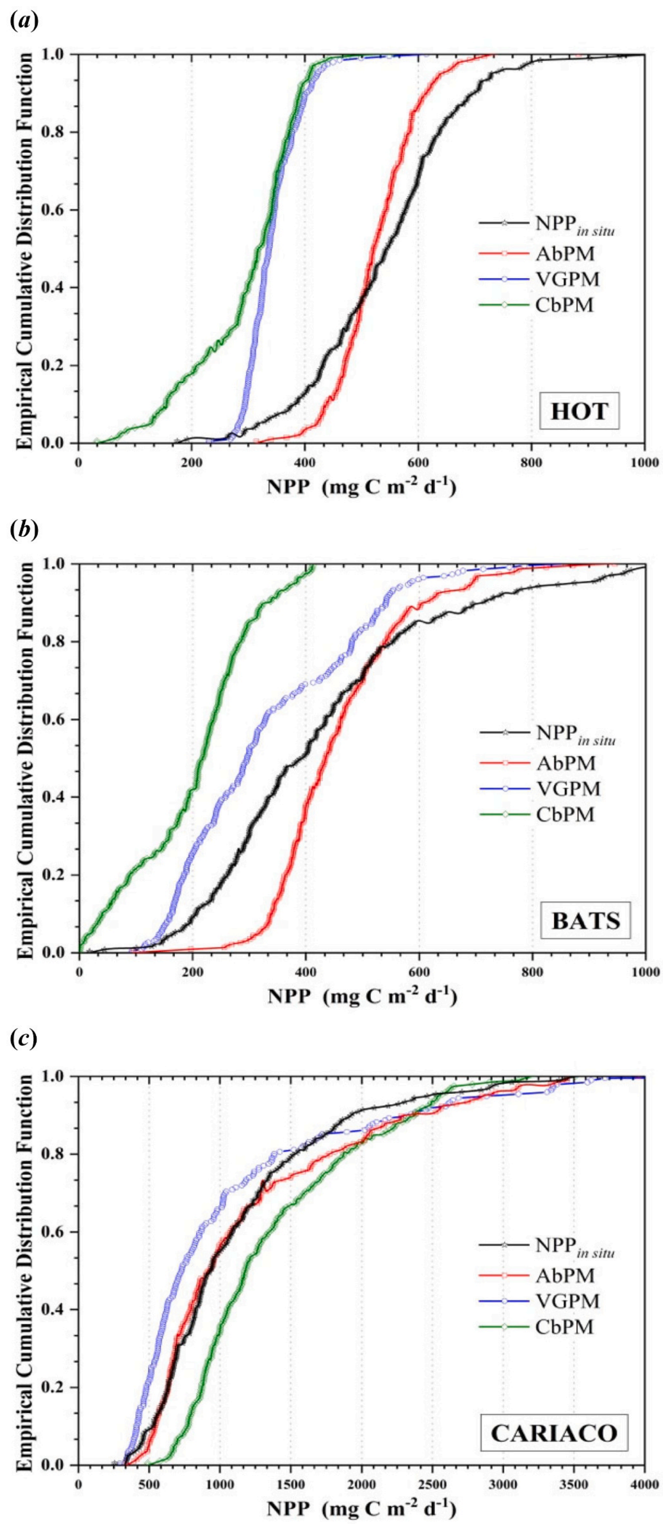

Fig. 8. Empirical cumulative distribution function (ECDF) of NPP_{insitu}, NPP_{AbPM}, NPP_{VGPM}, and NPP_{CbPM}. (*a*) HOT, (*b*) BATS, and (*c*) CARIACO.

larger areas, as was shown in Wu et al. (2022) for the complex water masses around the Korean peninsula.

CRediT authorship contribution statement

Jinghui Wu: Writing – review & editing, Writing – original draft, Formal analysis, Data curation. **Zhongping Lee:** Writing – review & editing, Supervision, Conceptualization. **Joaquim Goes:** Writing – review & editing, Supervision, Funding acquisition, Conceptualization. **Helga do R. Gomes:** Writing – review & editing, Formal analysis. **Jianwei Wei:** Writing – review & editing, Formal analysis.

Declaration of Competing Interest

The authors declare that they have no known competing financial interests or personal relationships that could have appeared to influence the work reported in this paper.

Data availability

All data related information (including website and code) are provided in the manuscript.

Acknowledgments

ZL is supported by the National Natural Science Foundation of China (#41830102, #41941008, #41890803). JW, JIG and HRG are supported by NASA Grants NNX16AD39GGEOCAPE, #NNH18ZDA00-CMS, #80LARC21DA002-GLIMR-AABO8078, NOAA GST SA18-CUNY-09 JAXA Grant JX-PSPC-550431, NSF-NNA 2220565 and New York Sea Grant LI96244421-0. We are especially grateful to the team of investigators from HOT, BATS and CARIACO stations, for their efforts in collecting and making available the long-term time-series of NPP. We are thankful to Dr. Mike Behrenfeld and Dr. Toby Westberry for making their code in estimating NPP following VGPM and CbPM publicly available. We are also thankful to the editor and two anonymous reviewers for their constructive suggestions for improving this manuscript.

Appendix A. Supplementary data

Supplementary data to this article can be found online at https://doi.org/10.1016/j.rse.2023.113983.

References

Antoine, D., Morel, A., 1996. Oceanic primary production 1. Adaptation of a spectral light~photosynthesis model in view of application to satellite chlorophy observations. Glob. Biogeochem. Cycles 10, 43–55.

Bailey, S.W., Werdell, P.J., 2006. A multi-sensor approach for the on-orbit validation of ocean color satellite data products. Remote Sens. Environ. 102, 12–23.

Barnes, M.K., Tilstone, G.H., Smyth, T.J., Suggett, D.J., Astoreca, R., Lancelot, C., Kromkamp, J.C., 2014. Absorption-based algorithm of primary production for total and size-fractionated phytoplankton in coastal waters. Mar. Ecol. Prog. Ser. 504, 73–89.

Behrenfeld, M.J., Falkowski, P.G., 1997. A consumer's guide to phytoplankton primary productivity models. Limnol. Oceanogr. 42, 1479–1491.

Behrenfeld, M.J., Boss, E., Siegel, D.A., Shea, D.M., 2005. Carbon-Based Ocean productivity and phytoplankton physiology from space. Glob. Biogeochem. Cycles 19.

Belo Couto, A., Brotas, V., Mélin, F., Groom, S., Sathyendranath, S., 2016. Inter-comparison of OC-CCI chlorophyll-a estimates with precursor data sets. Int. J. Remote Sens. 37, 4337–4355.

Boyce, D.G., Lewis, M.R., Worm, B., 2010. Global phytoplankton decline over the past century. Nature 466, 591–596.

Boyd, P., Trull, T., 2007. Understanding the export of biogenic particles in oceanic waters: is there consensus? Prog. Oceanogr. 72, 276–312.

Boyd, P.W., Claustre, H., Levy, M., Siegel, D.A., Weber, T., 2019. Multi-faceted particle pumps drive carbon sequestration in the ocean. Nature 568, 327–335.

Brewin, R.J., Sathyendranath, S., Platt, T., Bouman, H., Ciavatta, S., Dall'Olmo, G., Dingle, J., Groom, S., Jönsson, B., Kostadinov, T.S., 2021. Sensing the ocean biological carbon pump from space: A review of capabilities, concepts, research gaps and future developments. Earth Sci. Rev. 217, 103604.

Brewin, R.J., Sathyendranath, S., Kulk, G., Rio, M.-H., Concha, J.A., Bell, T.G., Bracher, A., Fichot, C., Frölicher, T.L., Galí, M., 2023. Ocean carbon from space: current status and priorities for the next decade. Earth Sci. Rev. 104386.

Campbell, J., Antoine, D., Armstrong, R., Arrigo, K., Balch, W., Barber, R., Behrenfeld, M., Bidigare, R., Bishop, J., Carr, M.-E., Esaias, W., Falkowski, P., Hoepffner, N., Iverson, R., Kiefer, D., Lohrenz, S., Marra, J., Morel, A., Ryan, J., Vedernikov, V., Waters, K., Yentsch, C., Yoder, J., 2002. Comparison of algorithms for estimating ocean primary production from surface chlorophyll, temperature, and irradiance. Glob. Biogeochem. Cycles 16 (9-1-9-15).

Carr, M.-E., Friedrichs, M.A.M., Schmeltz, M., Noguchi Aita, M., Antoine, D., Arrigo, K. R., Asanuma, I., Aumont, O., Barber, R., Behrenfeld, M., Bidigare, R., Buitenhuis, E. T., Campbell, J., Ciotti, A., Dierssen, H., Dowell, M., Dunne, J., Esaias, W., Gentili, B., Gregg, W., Groom, S., Hoepffner, N., Ishizaka, J., Kameda, T., Le Quéré, C., Lohrenz, S., Marra, J., Mélin, F., Moore, K., Morel, A., Reddy, T.E., Ryan, J., Scardi, M., Smyth, T., Turpie, K., Tilstone, G., Waters, K., Yamanaka, Y., 2006. A comparison of global estimates of marine primary production from ocean color. Deep-Sea Res. II Top. Stud. Oceanogr. 53, 741–770.

Chavez, F.P., Messie, M., Pennington, J.T., 2011. Marine primary production in relation to climate variability and change. Annu. Rev. Mar. Sci. 3, 227–260.

Church, M.J., Lomas, M.W., Muller-Karger, F., 2013. Sea change: charting the course for biogeochemical ocean time-series research in a new millennium. Deep-Sea Res. II Top. Stud. Oceanogr. 93, 2–15.

D'Alelio, D., Rampone, S., Cusano, L.M., Morfino, V., Russo, L., Sanseverino, N., Cloern, J.E., Lomas, M.W., 2020. Machine learning identifies a strong association between warming and reduced primary productivity in an oligotrophic ocean gyre. Sci. Rep. 10, 1–12.

Dave, A.C., Lozier, M.S., 2010. Local stratification control of marine productivity in the subtropical North Pacific. J. Geophys. Res. Oceans 115.

Doney, S.C., Fabry, V.J., Feely, R.A., Kleypas, J.A., 2009. Ocean Acidification: The Other CO2 Problem.

D'Ortenzio, F., Lavigne, H., Besson, F., Claustre, H., Coppola, L., Garcia, N., Laës-Huon, A., Le Reste, S., Malardé, D., Migon, C., Morin, P., Mortier, L., Poteau, A., Prieur, L., Raimbault, P., Testor, P., 2014. Observing mixed layer depth, nitrate and chlorophyll concentrations in the northwestern Mediterranean: A combined satellite and NO3 profiling floats experiment. Geophys. Res. Lett. 41, 6443–6451.

Ducklow, H.W., Doney, S.C., Steinberg, D.K., 2009. Contributions of long-term research and time-series observations to marine ecology and biogeochemistry. Annu. Rev. Mar. Sci. 1, 279–302.

Eppley, R.W., 1972. Temperature and phytoplankton growth in the sea. Fish. Bull. 70, 1063–1085.

Eppley, R.W., Peterson, B.J., 1979. Particulate organic matter flux and planktonic new production in the deep ocean. Nature 282, 677–680.

Eppley, R., Renger, E., 1988. Nanomolar increase in surface layer nitrate concentration following a small wind event. Deep Sea Res. Part A Oceanogr. Res. Pap. 35, 1119–1125.

Eppley, R., Steward, E., Abbott, M., Heyman, U., 1985. Estimating ocean primary production from satellite chlorophyll: introduction to regional differences and statistics for the southern California bight. J. Plankton Res. 7, 57–70. https://doi.org/10.1093/plankt/1097.1091.1057.

Falkowski, P.G., 1994. The role of phytoplankton photosynthesis in global biogeochemical cycles. Photosynth. Res. 39, 235–258.

Falkowski, P.G., 1998. Using satellite data to derive primary productivity in the world ocean. In: Hooker, S.B., Firestone, E.R. (Eds.), SeaWiFS Technical Report Series. NASA, Greenbelt, MD.

Field, C.B., Behrenfeld, M.J., Randerson, J.T., Falkowski, P., 1998. Primary production of the biosphere: integrating terrestrial and oceanic components. Science 281, 237–240.

Friedland, K.D., Stock, C., Drinkwater, K.F., Link, J.S., Leaf, R.T., Shank, B.V., Rose, J.M., Pilskaln, C.H., Fogarty, M.J., 2012. Pathways between primary production and fisheries yields of large marine ecosystems. PLoS One 7, e28945.

Friedrichs, M.A.M., Carr, M.-E., Barber, R.T., Scardi, M., Antoine, D., Armstrong, R.A., Asanuma, I., Behrenfeld, M.J., Buitenhuis, E.T., Chai, F., Christian, J.R., Ciotti, A.M., Doney, S.C., Dowell, M., Dunne, J., Gentili, B., Gregg, W., Hoepffner, N., Ishizaka, J., Kameda, T., Lima, I., Marra, J., Mélin, F., Moore, J.K., Morel, A., O'Malley, R.T., O'Reilly, J., Saba, V.S., Schmeltz, M., Smyth, T.J., Tjiputra, J., Waters, K., Westberry, T.K., Winguth, A., 2009. Assessing the uncertainties of model estimates of primary productivity in the tropical Pacific Ocean. J. Mar. Syst. 76, 113–133.

Garcia-Corral, L.S., Agustí, S., Regaudie-de-Gioux, A., Iuculano, F., Carrillo-de-Albornoz, P., Wassmann, P., Duarte, C.M., 2014. Ultraviolet radiation enhances Arctic net plankton community production. Geophys. Res. Lett. 41, 5960–5967.

Gregg, W.W., Rousseaux, C.S., 2019. Global Ocean primary production trends in the modern ocean color satellite record (1998–2015). Environ. Res. Lett. 14, 124011.

Gruber, N., Clement, D., Carter, B.R., Feely, R.A., Van Heuven, S., Hoppema, M., Ishii, M., Key, R.M., Kozyr, A., Lauvset, S.K., 2019. The oceanic sink for anthropogenic CO2 from 1994 to 2007. Science 363, 1193–1199.

Henson, S.A., Sanders, R., Madsen, E., Morris, P.J., Le Moigne, F., Quartly, G.D., 2011. A reduced estimate of the strength of the ocean's biological carbon pump. Geophys. Res. Lett. 38.

Hirawake, T., Takao, S., Horimoto, N., Ishimaru, T., Yamaguchi, Y., Fukuchi, M., 2011. A phytoplankton absorption-based primary productivity model for remote sensing in the Southern Ocean. Polar Biol. 34, 291–302.

Jolliff, J.K., Kindle, J.C., Shulman, I., Penta, B., Friedrichs, M.A.M., Helber, R., Arnone, R.A., 2009. Summary diagrams for coupled hydrodynamic-ecosystem model skill assessment. J. Mar. Syst. 76, 64–82.

Kahru, M., 2017. Ocean productivity from space: commentary. Glob. Biogeochem. Cycles 31, 214–216.

Karl, D.M., Letelier, R.M., Bidigare, R.R., Björkman, K.M., Church, M.J., Dore, J.E., White, A.E., 2021. Seasonal-to-decadal scale variability in primary production and particulate matter export at station ALOHA. Prog. Oceanogr. 195, 102563.

Kavanaugh, M.T., Church, M.J., Davis, C.O., Karl, D.M., Letelier, R.M., Doney, S.C., 2018. Aloha from the edge: reconciling three decades of in situ Eulerian observations and geographic variability in the north pacific subtropical gyre. Front. Mar. Sci. 5, 130.

Keeling, R.F., Körtzinger, A., Gruber, N., 2009. Ocean Deoxygenation in a Warming World.

Kiefer, D.A., Mitchell, B.G., 1983. A simple, steady state description of phytoplankton growth based on absorption cross section and quantum efficiency. Limnol. Oceanogr. 28, 770–776.

Knap, A.H., Michaels, A., Close, A.R., Ducklow, H., Dickson, A.G., 1996. Protocols for the Joint Global Ocean Flux Study (JGOFS) Core Measurements.

Koslow, J.A., Allen, C., 2011. The influence of the ocean environment on the abundance of market squid, Doryteuthis (Loligo) opalescens, paralarvae in the Southern California bight. CalCOFI Rep. 52, 205–213.

Krause, S., Hannah, D.M., Fleckenstein, J.H., 2009. Hyporheic hydrology: interactions at the groundwater-surface water interface. Hydrol, Process. 23, 2103–2107.

Krumhardt, K.M., Lovenduski, N.S., Long, M.C., Lindsay, K., 2017. Avoidable impacts of ocean warming on marine primary production: insights from the CESM ensembles. Glob. Biogeochem. Cycles 31, 114–133.

Kulk, G., Platt, T., Dingle, J., Jackson, T., Jönsson, B.F., Bouman, H.A., Babin, M., Brewin, R.J., Doblin, M., Estrada, M., 2020. Primary production, an index of climate change in the ocean: satellite-based estimates over two decades. Remote Sens. 12, 826.

Le Quéré, C., Andrew, R.M., Friedlingstein, P., Sitch, S., Hauck, J., Pongratz, J., Pickers, P.A., Korsbakken, J.I., Peters, G.P., Canadell, J.G., 2018. Global carbon budget 2018. Earth Syst. Sci. Data 10.

Lee, Z., Marra, J.F., 2022. The use of VGPM to estimate oceanic primary production: A "tango" difficult to dance. J. Remote Sens. 2022.

Lee, Z.P., Carder, K.L., Marra, J., Steward, R.G., Perry, M.J., 1996. Estimating primary production at depth from remote sensing. Appl. Opt. 35, 463–474.

Lee, Z., Carder, K.L., Mobley, C.D., Steward, R.G., Patch, J.S., 1999. Hyperspectral remote sensing for shallow waters: 2. Deriving bottom depths and water properties by optimization. Appl. Opt. 38, 3831–3843.

Lee, Z.P., Carder, K.L., Arnone, R.A., 2002. Deriving inherent optical properties from water color: a multi-band quasi-analytical algorithm for optically deep waters. Appl. Opt. 41 (27), 5755–5772.

Lee, Z., Shang, S., Hu, C., Lewis, M., Arnone, R., Li, Y., Lubac, B., 2010. Time series of bio-optical properties in a subtropical gyre: implications for the evaluation of interannual trends of biogeochemical properties. J. Geophys. Res. 115.

Lee, Z., Lance, V.P., Shang, S., Vaillancourt, R., Freeman, S., Lubac, B., Hargreaves, B.R., Castillo, C.D., Miller, R., Twardowski, M., Wei, G., 2011. An assessment of optical properties and primary production derived from remote sensing in the Southern Ocean (SO GasEx). J. Geophys. Res. *116* https://doi.org/10.1029/2010JC006747. C00F03.

Lee, Z.P., Hu, C., Shang, S., Du, K., Lewis, M., Arnone, R., Brewin, R., 2013. Penetration of UV-visible solar light in the global oceans: insights from ocean color remote sensing. J. Geophys. Res. 118, 4241–4255 (doi:4210.1002/jgrc.20308).

Lee, Y.J., Matrai, P.A., Friedrichs, M.A., Saba, V.S., Antoine, D., Ardyna, M., Asanuma, I., Babin, M., Belanger, S., Benoit-Gagne, M., Devred, E., Fernandez-Mendez, M., Gentili, B., Hirawake, T., Kang, S.H., Kameda, T., Katlein, C., Lee, S.H., Lee, Z., Melin, F., Scardi, M., Smyth, T.J., Tang, S., Turpie, K.R., Waters, K.J., Westberry, T. K., 2015a. An assessment of phytoplankton primary productivity in the Arctic Ocean from satellite ocean color/in situ chlorophyll-a based models. J. Geophys. Res. Oceans 120, 6508–6541.

Lee, Z., Marra, J., Perry, M.J., Kahru, M., 2015b. Estimating oceanic primary productivity from ocean color remote sensing: A strategic assessment. J. Mar. Syst. 149, 50–59.

Loisel, H., Meriaux, X., Berthon, J.F., Poteau, A., 2007. Investigation of the optical backscattering to scattering ratio of marine particles in relation to their biogeochemical composition in the eastern English Channel and southern North Sea. Limnol. Oceanogr. 52, 739–752.

Lomas, M., Bates, N., Johnson, R., Knap, A., Steinberg, D., Carlson, C., 2013. Two decades and counting: 24-years of sustained open ocean biogeochemical measurements in the Sargasso Sea. Deep-Sea Res. II Top. Stud. Oceanogr. 93, 16–32.

Lomas, M.W., Bates, N.R., Johnson, R.J., Steinberg, D.K., Tanioka, T., 2022. Adaptive carbon export response to warming in the Sargasso Sea. Nat. Commun. 13, 1211.

Lorenzoni, L., Toro-Farmer, G., Varela, R., Guzman, L., Rojas, J., Montes, E., Muller-Karger, F., 2015. Characterization of phytoplankton variability in the Cariaco Basin using spectral absorption, taxonomic and pigment data. Remote Sens. Environ. 167, 259–268.

Ma, S., Tao, Z., Yang, X., Yu, Y., Zhou, X., Ma, W., Li, Z., 2014. Estimation of marine primary productivity from satellite-derived phytoplankton absorption data. IEEE J. Select. Topics Appl. Earth Observ. Remote Sens. 7, 3084–3092.

Marra, J., 2002. Approaches to the measurement of plankton production. In: Williams, P. J.B., Thomas, D.N., Reynolds, C.S. (Eds.), Phytoplankton Productivity: Carbon Assimilation in Marine and Freshwater Ecosystems. Blackwell, Cambridge, U. K. https://doi.org/10.1002/9780470995204.ch9780470995204.

Marra, J., Ho, C., Trees, C., 2003. An Alternative Algorithm for the Calculation of Primary Productivity from Remote Sensing Data. Lamont-Doherty Earth Observatory of Columbia University, pp. 1–27.

Morel, A., 1991. Light and marine photosynthesis: a spectral model with geochemical and climatological implications. Prog. Oceanogr. 26, 263–306.

Muller-Karger, F.E., Astor, Y.M., Benitez-Nelson, C.R., Buck, K.N., Fanning, K.A., Lorenzoni, L., Montes, E., Rueda-Roa, D.T., Scranton, M.I., Tappa, E., 2019. The scientific legacy of the CARIACO Ocean time-series program. Annu. Rev. Mar. Sci. 11, 413–437.

Perry, M.J., 1986. Assessing marine primary productiofronm space. BioScience 36, 461–467.

Pinkerton, M.H., Boyd, P.W., Deppeler, S., Hayward, A., Höfer, J., Moreau, S., 2021. Evidence for the impact of climate change on primary producers in the Southern Ocean. Front. Ecol. Evol. 9, 592027.

Platt, T., 1986. Primary production of ocean water column as a function of surface light intensity: algorithms for remote sensing. Deep-Sea Res. 33, 149–163.

Platt, T., Sathyendranath, S., 1988. Oceanic primary production: estimation by remote sensing at local and regional scales. Science 241, 1613–1620.

Platt, T., Gallegos, C.L., Harrison, W.G., 1980. Photoinhibition of photosynthesis in natural assemblages of marine phytoplankton. J. Mar. Res. 38, 687–701.

Randolph, K., Dierssen, H.M., Twardowski, M., Cifuentes-Lorenzen, A., Zappa, C.J., 2014. Optical measurements of small deeply penetrating bubble populations generated by breaking waves in the Southern Ocean. J. Geophys. Res. Oceans 119, 757–776.

Regaudie-de-Gioux, A., Huete-Ortega, M., Sobrino, C., López-Sandoval, D., González, N., Fernández-Carrera, A., Vidal, M., Marañón, E., Cermeño, P., Latasa, M., 2019. Multi-model remote sensing assessment of primary production in the subtropical gyres. J. Mar. Syst. 196, 97–106.

Reid, P.C., Fischer, A.C., Lewis-Brown, E., Meredith, M.P., Sparrow, M., Andersson, A.J., Antia, A., Bates, N.R., Bathmann, U., Beaugrand, G., 2009. Impacts of the oceans on climate change. Adv. Mar. Biol. 56, 1–150.

Rousseaux, C.S., Gregg, W.W., 2015. Recent decadal trends in global phytoplankton composition. Glob. Biogeochem. Cycles 29, 1674–1688.

Saba, V.S., Friedrichs, M.A.M., Carr, M.-E., Antoine, D., Armstrong, R.A., Asanuma, I., Aumont, O., Bates, N.R., Behrenfeld, M.J., Bennington, V., Bopp, L., Bruggeman, J., Buitenhuis, E.T., Church, M.J., Ciotti, A.M., Doney, S.C., Dowell, M., Dunne, J., Dutkiewicz, S., Gregg, W., Hoepffner, N., Hyde, K.J.W., Ishizaka, J., Kameda, T., Karl, D.M., Lima, I., Lomas, M.W., Marra, J., McKinley, G.A., Mélin, F., Moore, J.K., Morel, A., O'Reilly, J., Salihoglu, B., Scardi, M., Smyth, T.J., Tang, S., Tjiputra, J., Uitz, J., Vichi, M., Waters, K., Westberry, T.K., Yool, A., 2010. Challenges of modeling depth-integrated marine primary productivity over multiple decades: A case study at BATS and HOT. Glob. Biogeochem. Cycles 24 (n/a-n/a).

Saba, V.S., Friedrichs, M.A.M., Antoine, D., Armstrong, R.A., Asanuma, I., Behrenfeld, M.J., Ciotti, A.M., Dowell, M., Hoepffner, N., Hyde, K.J.W., Ishizaka, J., Kameda, T., Marra, J., Mélin, F., Morel, A., O'Reilly, J., Scardi, M., Smith, W.O., Smyth, T.J., Tang, S., Uitz, J., Waters, K., Westberry, T.K., 2011. An evaluation of ocean color model estimates of marine primary productivity in coastal and pelagic regions across the globe. Biogeosciences 8, 489–503.

Sathyendranath, S., Platt, T., 1995. Remote sensing of water-column primary production. In: Li, W.K.W., Maestrini (Eds.), Measurement of Primary Production from the Molecular to the Global Scale. ICES Marine Science Symposia, Copenhagen, pp. 236–243.

Sathyendranath, S., Brewin, R.J., Brockmann, C., Brotas, V., Calton, B., Chuprin, A., Cipollini, P., Couto, A.B., Dingle, J., Doerffer, R., 2019. An ocean-colour time series for use in climate studies: the experience of the ocean-colour climate change initiative (OC-CCI). Sensors 19, 4285.

Sathyendranath, S., Platt, T., Kovač, Ž., Dingle, J., Jackson, T., Brewin, R.J., Franks, P., Marañón, E., Kulk, G., Bouman, H.A., 2020. Reconciling models of primary production and photoacclimation. Appl. Opt. 59, C100–C114.

Shih, Y.-Y., Shiah, F.-K., Lai, C.-C., Chou, W.-C., Tai, J.-H., Wu, Y.-S., Lai, C.-Y., Ko, C.-Y., Hung, C.-C., 2021. Comparison of primary production using in situ and satellite-derived values at the SEATS station in the South China Sea. Front. Mar. Sci. 8, 747–763.

Siegel, D., Buesseler, K., Doney, S., Sailley, S., Behrenfeld, M.J., Boyd, P., 2014. Global assessment of ocean carbon export by combining satellite observations and food-web models. Glob. Biogeochem. Cycles 28, 181–196.

Song, L., Lee, Z., Shang, S., Huang, B., Wu, J., Wu, Z., Lu, W., Liu, X., 2023. On the spatial and temporal variations of primary production in the South China Sea. IEEE Trans. Geosci. Remote Sens. 61, 1–14.

Steemann Nielsen, E., 1952. The use of radio-active carbon (c14) for measuring organic production in the sea. ICES J. Mar. Sci. 18, 24.

Steinberg, D.K., Carlson, C.A., Bates, N.R., Johnson, R.J., Michaels, A.F., Knap, A.H., 2001. Overview of the US JGOFS Bermuda Atlantic time-series study (BATS): a decade-scale look at ocean biology and biogeochemistry. Deep-Sea Res. II Top. Stud. Oceanogr. 48, 1405–1447.

Stramski, D., Boss, E., Bogucki, D., Voss, K.J., 2004. The role of seawater constituents in light backscattering in the ocean. Prog. Oceanogr. 61, 27–56.

Stramski, D., Reynolds, R.A., Babin, M., Kaczmarek, S., Lewis, M.R., Röttgers, R., Sciandra, A., Stramska, M., Twardowski, M.S., Franz, B.A., Claustre, H., 2008. Relationships between the surface concentration of particulate organic carbon and optical properties in the eastern South Pacific and eastern Atlantic oceans. Biogeosciences 5, 171–201.

Taylor, K.E., 2001. Summarizing multiple aspects of model performance in a single diagram. J. Geophys. Res. Atmos. 106, 7183–7192.

Werdell, P.J., Franz, B.A., Bailey, S.W., Feldman, G.C., Boss, E., Brando, V.E., Dowell, M., Hirata, T., Lavender, S.J., Lee, Z., Loisel, H., Maritorena, S., Mélin, F., Moore, T.S., Smyth, T.J., Antoine, D., Devred, E., d'Andon, O.H.F., Mangin, A., 2013. Generalized Ocean color inversion model for retrieving marine inherent optical properties. Appl. Opt. 52, 2019–2037.

Westberry, T., Behrenfeld, M.J., Siegel, D.A., Boss, E., 2008. Carbon-based primary productivity modeling with vertically resolved photoacclimation. Glob. Biogeochem. Cycles 22. https://doi.org/10.1029/2007GB003078.

Westberry, T.K., Silsbe, G.M., Behrenfeld, M.J., 2023. Gross and net primary production in the global ocean: an ocean color remote sensing perspective. Earth Sci. Rev. 104322.

Wu, J., Lee, Z., Xie, Y., Goes, J., Shang, S., Marra, J.F., Lin, G., Yang, L., Huang, B., 2021. Reconciling between optical and biological determinants of the euphotic zone depth. J. Geophys. Res. Oceans 126 (e2020JC016874).

Wu, J., Goes, J.I., do Rosario Gomes, H., Lee, Z., Noh, J.-H., Wei, J., Shang, Z., Salisbury, J., Mannino, A., Kim, W., 2022. Estimates of diurnal and daily net primary productivity using the Geostationary Ocean color imager (GOCI) data. Remote Sens. Environ. 280, 113183.

Zhang, X.D., Lewis, M., Johnson, B., 1998. Influence of bubbles on scattering of light in the ocean. Appl. Opt. 37, 6525–6536.

Zhang, S., Curchitser, E.N., Kang, D., Stock, C.A., Dussin, R., 2018. Impacts of mesoscale eddies on the vertical nitrate flux in the Gulf stream region. J. Geophys. Res. Oceans 123, 497–513.

Zoffoli, M.L., Lee, Z., Marra, J.F., 2018. Regionalization and dynamic parameterization of quantum yield of photosynthesis to improve the ocean primary production estimates from remote sensing. Front. Mar. Sci. 5, 446.